Monthly Notices
of the
ROYAL ASTRONOMICAL SOCIETY

MNRAS **508,** 1929–1946 (2021)
Advance Access publication 2021 September 21

https://doi.org/10.1093/mnras/stab2676

The Galactic neutron star population – I. An extragalactic view of the Milky Way and the implications for fast radio bursts

A. A. Chrimes [1★] A. J. Levan,[1,2] P. J. Groot,[1,3,4] J. D. Lyman [2] and G. Nelemans[1,5,6]

[1]*Department of Astrophysics/IMAPP, Radboud University Nijmegen, PO Box 9010, NL-6500 GL Nijmegen, the Netherlands*
[2]*Department of Physics, University of Warwick, Coventry CV4 7AL, UK*
[3]*Inter-University Institute for Data Intensive Astronomy, Department of Astronomy, University of Cape Town, Private Bag X3, 7701 Rondebosch, South Africa*
[4]*South African Astronomical Observatory, PO Box 9, 7935 Observatory, South Africa*
[5]*Institute for Astronomy, KU Leuven, Celestijnenlaan 200D bus 2401, 3001 Leuven, Belgium*
[6]*SRON, Netherlands Institute for Space Research, Sorbonnelaan 2, NL-3584 CA Utrecht, the Netherlands*

Accepted 2021 September 15. Received 2021 September 15; in original form 2021 May 10

ABSTRACT

A key tool astronomers have to investigate the nature of extragalactic transients is their position on their host galaxies. Galactocentric offsets, enclosed fluxes, and the fraction of light statistic are widely used at different wavelengths to help infer the nature of transient progenitors. Motivated by the proposed link between magnetars and fast radio bursts (FRBs), we create a face-on image of the Milky Way using best estimates of its size, structure, and colour. We place Galactic magnetars, pulsars, low-mass, and high-mass X-ray binaries on this image, using the available distance information. Galactocentric offsets, enclosed fluxes, and fraction of light distributions for these systems are compared to extragalactic transient samples. We find that FRBs follow the distributions for Galactic neutron stars closest, with 24 (75 per cent) of the Anderson–Darling tests we perform having a p-value greater than 0.05. This suggests that FRBs are located on their hosts in a manner consistent with Galactic neutron stars on the Milky Way's light, although we cannot determine which specific neutron star population is the best match. The Galactic distributions are consistent with other extragalactic transients much less often across the range of comparisons made, with type Ia SNe in second place, at only 33 per cent of tests exceeding 0.05. Overall, our results provide further support for FRB models invoking isolated young neutron stars, or binaries containing a neutron star.

Key words: stars: magnetars – stars: neutron – supernovae: general – Galaxy: structure – fast radio bursts.

1 INTRODUCTION

Several classes of astrophysical transients are associated with neutron stars, ranging from their formation in core-collapse supernovae (CC-SNe) to their mergers in short γ-ray bursts (GRBs). Magnetars are a subset of neutron stars (Duncan & Thompson 1992), distinguished by their extreme magnetic fields (10^{14}–10^{15} G), high radio/X-ray/γ-ray luminosities despite spin-down luminosities comparable to pulsars (Thompson & Duncan 1996; Kouveliotou et al. 1998), and young characteristic ages of $\sim 10^3$–10^5 yr (Olausen & Kaspi 2014). Magnetars are observed in the Milky Way and Magellenic clouds as soft γ repeaters (SGRs; Mazets, Golenetskij & Guryan 1979a; Mazets et al. 1979b) and anomalous X-ray pulsars (Fahlman & Gregory 1981), detectable primarily through their high-energy flares, and in some cases persistent emission (Olausen & Kaspi 2014). Giant magnetar flares, detectable at extragalactic distances, have been identified as an alternative origin for some short GRBs (Hurley et al. 2005; Ofek et al. 2006, 2008; Burns et al. 2021; Svinkin et al. 2021). Magnetars have also been invoked as central engines in superluminous supernovae (SLSNe; Kasen & Bildsten 2010; Woosley 2010) and GRBs (Metzger, Quataert & Thompson 2008; Metzger et al. 2011). More recently, they have become a promising explanation for the fast radio burst (FRB) phenomenon.

This paper is partly motivated by the FRB–magnetar connection, following the detection of FRB-like bursts from the Galactic magnetar SGR 1935+2154 (hereafter SGR 1935; Bochenek et al. 2020; CHIME/FRB Collaboration 2020). Although the SGR 1935 bursts are fainter than extragalactic FRBs, they are orders of magnitude brighter than other radio transients with comparable frequencies and millisecond durations (e.g. pulsar pulses; Keane 2018). Even before this detection, magnetar flaring was a leading theory among the dozens offered to explain FRBs (Platts et al. 2019).[1] See also Chatterjee (2020), Baring et al. (2020), Xiao, Wang & Dai (2021), and Zhang (2020) for reviews. Despite this association, there are still open questions around the relationship between the X-ray/γ-ray and radio emission (Katz 2016; De et al. 2020a; Lin et al. 2020; Bailes et al. 2021; Li et al. 2021; Ridnaia et al. 2021; Tavani et al. 2021; Verrecchia et al. 2021; Younes et al. 2021). It is unclear if all FRBs repeat, or if there are two distinct populations of single and repeating events. Results from the first CHIME/FRB catalogue (Pleunis et al. 2021; The CHIME/FRB Collaboration et al. 2021) suggest that bursts from repeaters have larger temporal widths and narrow bandwidths, although the origin of this difference is currently uncertain. The

★ E-mail: a.chrimes@astro.ru.nl

[1] frbtheorycat.org/index.php/Main_Page

nature of the weak periodicity/clustering seen in repeating FRB bursts also remains to be understood (Beniamini, Wadiasingh & Metzger 2020; Pastor-Marazuela et al. 2020; Li & Zanazzi 2021), although claims of similar periodicity have now also been made for SGR 1935 (Grossan 2021).

If we assume that FRBs are caused by magnetar flares, and that SGR 1935 produces FRBs, then we must conclude that the Milky Way is an FRB host galaxy. If we also assume that all magnetars are capable of producing FRBs, then it follows that the distribution of FRBs on their host galaxies should match the distribution of magnetars on the Milky Way, at least for morphologically similar spiral galaxies. FRB sample size increases (now ∼600 single FRBs and 20 repeaters; The CHIME/FRB Collaboration 2021) have led to more host identifications (Eftekhari & Berger 2017; Heintz et al. 2020),[2] and consequently, population studies of these hosts have now begun.

One way to study transient hosts is through their spectral energy distributions (SEDs), from which SED fitting can be used to infer the constituent stellar populations. Such work has found that FRB hosts span a range of masses and star formation rates (SFRs), and correspondingly, morphological types. The mean stellar mass is around $\sim 10^{10}\,\mathrm{M}_{\odot}$, and SFRs are typically moderate ∼0.1–$1\,\mathrm{M}_{\odot}\,\mathrm{yr}^{-1}$ (Bhandari et al. 2020; Heintz et al. 2020; Li & Zhang 2020), comparable to the Milky Way. These properties disfavour very massive stellar progenitors, such as those of SLSNe and long GRBs, but are consistent with regular CCSN hosts. To complicate matters further, Fong et al. (2021) find that the host galaxy of FRB 20201124A assembled >90 per cent of its stellar mass >1 Gyr ago, perhaps favouring a long delay time progenitor. Even more striking was the identification of a repeating FRB in an M81 globular cluster (Kirsten et al. 2021), for which an old underlying population is overwhelmingly likely. Such scenarios are not straightforward to ascribe to magnetars given their young ages, and presumed origin in massive stars, although alternative models invoking accretion-induced collapse have been put forward (e.g. Usov 1992; Levan et al. 2006).

The projected offset of transients from their host centre is another commonly used measure. At its most basic level, galaxies tend to have SFR gradients such that more star formation occurs towards the centre (neglecting metallicity effects and morphological differences). Furthermore, large offsets can provide insight into natal kicks, most prominently seen in short GRBs (Fong, Berger & Fox 2010; Church et al. 2011; Tunnicliffe et al. 2014). Heintz et al. (2020) and Mannings et al. (2021) measure the physical offsets δr of FRBs from their hosts, and also the normalized offsets $\delta r/r_{\mathrm{e}}$, where r_{e} is the half-light radius. Using the normalized offset accounts for different radial intensity profiles (for example, the underlying stellar mass at a given offset can be different in two otherwise identical galaxies, if their physical size and compactness differ). Heintz et al. (2020) and Mannings et al. (2021) find that CCSNe, SGRBs, and type Ia SNe are the most consistent with FRB offsets.

We can also measure the enclosed fraction of total galaxy flux within the galactocentric radius of the transient (James & Anderson 2006; Anderson & James 2009; Anderson et al. 2015; Audcent-Ross et al. 2020). A cumulative distribution of the fractional enclosed fluxes will produce a 1:1 relation if the transient traces the light. Mannings et al. (2021) calculate this distribution for eight FRBs on their hosts in the infrared (IR), again finding consistency with a stellar mass tracing progenitor.

[2] frbhosts.org/

Another metric is the fraction of light (F_{light}; Fruchter et al. 2006). This technique ranks host-associated pixels and normalizes their cumulative distribution, such that the brightest pixel on a galaxy is assigned the value 1, representing the cumulative fraction of total host flux in regions of surface brightness 'below' the pixel that contains the transient. Unbiased tracers of light sample F_{light} values uniformly, whereas biased data sets over/undersample from brighter/fainter pixels. Different wavelengths are used to probe different stellar populations: shorter, UV/blue bands trace young stars and thus star formation, IR/red bands better trace older stars and stellar mass. Mannings et al. (2021) compute F_{light} for eight FRB hosts using UVIS and IR *Hubble Space Telescope*/WFC3 data. They compare to other transients, finding that type Ia SNe and SGRBs are the best match, but noting that the uncertainties are large. Nevertheless, this result suggests a stellar mass tracing progenitor.

As magnetars have been suggested as both the source of FRBs, and as the central engines/remnants of SLSNe and GRBs, there have been several targeted radio searches at the locations of recently (i.e. in the last few decades) observed transients. Searches of this nature have yet to detect an FRB (Metzger, Berger & Margalit 2017; Hilmarsson et al. 2020; Mondal et al. 2020; Palliyaguru et al. 2021), but deep optical searches have been able to rule out an association between FRBs and SLSNe/bright SNe Ia, GRB afterglows and tidal disruption events, on time-scales of 1 d to 1 yr post-burst (Nuñez et al. 2021).

A final method to explore the nature of FRB progenitors is to compare their redshift distribution to the cosmic SFR history. FRB population synthesis has again found conflicting results, with some work finding that their rate is consistent with the SFR (and therefore magnetar production; Gardenier & van Leeuwen 2021; James et al. 2021), and others claiming that they better trace stellar mass (Luo et al. 2020).

As can be seen from this overview of host populations, offsets (host level and resolved), F_{light}, targeted searches for new FRB sources, and redshift distribution studies, the sole origin of FRBs in giant magnetar flares is still far from certain. Indeed, these results have led to conflicting interpretations over whether magnetars can explain all FRBs (Safarzadeh et al. 2020; Bochenek, Ravi & Dong 2021), and if so, what the progenitor channels should be (Margalit, Berger & Metzger 2019; Margalit et al. 2020). Our comparison of magnetar (and other neutron star) positions in the Milky Way, versus FRBs locations within their hosts, is therefore a valuable alternative diagnostic.

The aims of this paper require the ability to map both the Milky Way itself, and the neutron star populations within. Galactic magnetars have been studied in detail, in terms of their distances, activity, magnetic fields, ages, and more (Olausen & Kaspi 2014; Beniamini et al. 2019); pulsar (Manchester et al. 2005; Yao, Manchester & Wang 2017) and X-ray binary (XRB) catalogues are also maintained (Kretschmar et al. 2019; Sazonov et al. 2020). Much of the previous literature has focused on modelling the Galaxy and neutron star populations in a statistical sense (e.g. Sartore et al. 2010; Sharma et al. 2011), or if measured remnant positions are used, in terms of longitude, latitude, or scale height distributions (van Paradijs & White 1995; White & van Paradijs 1996; Jonker & Nelemans 2004; Manchester et al. 2005; Olausen & Kaspi 2014; Repetto, Igoshev & Nelemans 2017; Verberne & Vink 2021). However, there have been some attempts to measure correlations between neutron stars and Galactic structures in the plane of the Galaxy (e.g. clustering between OB associations and high-mass XRBs; Bodaghee et al. 2012; Coleiro & Chaty 2013). Crucially, it is now possible to map spiral arms and star-forming complexes (SFCs) throughout the Milky Way using masers (Reid et al. 2014, 2016, 2019). Doing this at other

Table 1. The Galactic neutron star samples used in this work. Listed are the source reference, initial sample size, size following a luminosity cut (if applicable), and the final size, after restricting the sample to $y < 8.3$ kpc and removing objects in the Magellenic clouds (if previously included).

Population	Source	Init. size	Subset with d estimate	Luminosity cut	Size after L cut	Final size after $y < 8.3$kpc cut
Magnetars	McGill – Olausen & Kaspi (2014)	31	26	–	26	20
Pulsars	ANTF – Manchester et al. (2005)	2872	2822	>65 mJy kpc^2	229	127
LMXBs	INTEGRAL – Sazonov et al. (2020)	166	119	–	119	84
HMXBs	INTEGRAL – Kretschmar et al. (2019)	64	57	–	57	36

wavelengths, such as the optical, is difficult due to dust extinction, particularly further away from the Solar neighbourhood (e.g. Russeil 2003; Hou & Han 2014; Gaia Collaboration 2016). There have also been studies looking at Milky Way global properties in the context of Milky Way analogues (e.g. Licquia, Newman & Brinchmann 2015). With precise localizations and distance estimates, we can now see how neutron stars would appear distributed on the Milky Way, if viewed externally.

This paper is motivated by the magnetar–FRB connection, and as such there is a focus on magnetars and FRBs. However, studying how neutron stars are distributed throughout the Milky Way has a wider ranging relevance, for many classes of core-collapse and merger transients. This will be the focus of a follow-up paper in this series.

This paper is structured as follows. In Section 2, the Galactic magnetar, pulsar, and XRB samples are described. Section 3 describes how the basic components of the Milky Way are assembled in order to produce a face-on 'image' of the Galaxy. The neutron star projected offsets, host-normalized offsets, and enclosed fluxes on the face-on disc of the Milky Way are discussed in Section 4. Fraction of light measurements follows in Section 5. The arm offsets, host offsets, enclosed fluxes, and fraction of light distributions are compared to samples of extragalactic transients in these sections. Section 6 presents a summary of the results and their implications, followed by concluding remarks in Section 7.

2 MAPPING NEUTRON STARS IN THE MILKY WAY

Neutron stars can be identified observationally in several ways. Here, we use publicly available catalogues for four categories of neutron star/systems containing neutron stars. These are magnetars, including soft gamma repeaters (SGRs) and anomalous X-ray pulsars (AXPs; Olausen & Kaspi 2014), pulsars (including binaries and millisecond pulsars; Manchester et al. 2005), and XRBs (high and low mass; Kretschmar et al. 2019; Sazonov et al. 2020). These initial catalogues are reduced by selecting those sources with a distance estimate, and a luminosity cut is also applied to the pulsars, for increased uniformity of coverage across the Galaxy.

The samples are then restricted to the half of the Galaxy this side of Galactic Centre (GC). This is because the neutron star samples have biases against detection at large distances, particularly towards and beyond GC. Distance uncertainties also tend to be larger further away, for example, *Gaia* parallax-inferred distances (for XRBs) can only be estimated in the local 4–5 kpc. GC is approximately 8 kpc away (e.g. Gravity Collaboration 2019), but throughout this paper we adopt a y-coordinate cut-off of <8.3 kpc (we define the y-axis as parallel to the Sun–GC line in a face-on Galactic coordinate system, with the Sun at 0 and GC at 8.3 kpc). This cut approximately halves the galaxy at GC but ensures that the centrally located magnetar SGR 1745−2900 is not excluded from any distributions. This would be unrepresentative given that we know of at least one magnetar in the central ∼100 pc of the Galaxy. Because we expect that Galactic populations on our side, versus the other side, of GC should be similar, these half-Galaxy samples should be broadly representative of the Galaxy as a whole. Any objects in the Magellenic clouds are also removed in this final cut.

The input catalogues, cuts, and final samples used are summarized in Table 1. We now describe each neutron star data set in turn.

2.1 Magnetars

We use the McGill magnetar catalogue of Olausen & Kaspi (2014). The distances for each source are the most recent values in the literature, and the reasoning for each distance is listed in table 7 of Olausen & Kaspi (2014). These include estimating the distance to an associated supernova remnant (SNR), using the tip of the red giant branch in associated clusters, and X-ray inferred column densities. Heliocentric distances and uncertainties are given by the upper and lower values listed in the McGill catalogue (and distance references therein). Where an uncertainty has not been quantified, a 15 per cent error on the distance is assumed, the mean of the uncertainties that are available.

The distance for SGR 1935 is highly uncertain, with estimates from dispersion measures, dust extinction, a potentially associated SNR, and nearby molecular clouds (see Bailes et al. 2021, for an overview). We adopt the Bailes et al. (2021) best distance estimate of 6.5 kpc, with a lower limit from their dispersion measure/dust analysis of 1.2 kpc, and an upper limit of 9.5 kpc the value assumed by Bochenek et al. (2020).

Although the lack of a strong local bias in the magnetar sample suggests that selection effects are not significant (Olausen & Kaspi 2014), there is a dearth of magnetars on the far side of the GC. This is despite the fact that γ-ray observatories have sufficient sensitivity to detect giant magnetar flares at extragalactic distances (Burns et al. 2021). A similar effect has been noted before in the X-ray binary population (Jonker & Nelemans 2004), although in that case, detections are in softer X-rays that are more liable to H I absorption and source confusion effects that preferentially occur along sightlines towards the GC.

There are three possibilities: that many of the magnetars have misassigned distances, that the sample really is incomplete, or that the effect is real and there are fewer magnetars on the far side of the Galaxy (unlikely, given that spiral galaxies tend not to have large-scale asymmetries of this nature). Beniamini et al. (2019) discuss the Milky Way magnetar sample, explaining that calculating completeness is non-trivial when SGRs are detected in different modes (quiescence versus flaring) with different observatories. They conclude that the missing fraction is around 0.3 for currently active magnetars. Similarly, Gullón et al. (2015) find that the Galactic X-ray pulsar population is complete above an absorbed flux of 3×10^{-12} erg s^{-1} cm^{-2}. The sample used is therefore unlikely to be seriously incomplete for currently active sources this side of

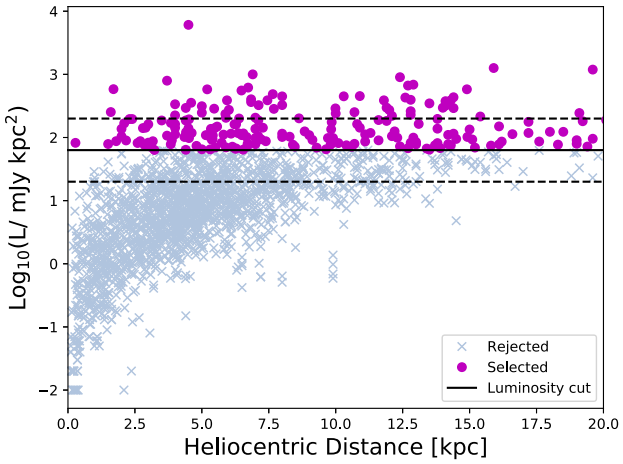

Figure 1. ATNF catalogue pulsar 1.4 GHz luminosities versus the best distance estimates. A cut is applied at 65 mJy kpc^2, which removes much of the strong local disc bias in the sample and gives (approximately, with the exception of the GC) equal coverage across the Galaxy. Two alternative cuts ($\pm$0.5 dex) are shown by dashed lines, these are later used to demonstrate the impact of different choices. Selecting the most luminous pulsars slightly shifts the sample towards younger sources – in $\log_{10}$(age/yr), the full sample has a median and standard deviation of 6.8 ± 1.4, compared to 6.5 ± 0.9 for the bright pulsars.

GC. The magnetars in the final sample are listed in Table A1 of Appendix A.

2.2 Pulsars

For pulsars, we use the ATNF catalogue (version 1.64; Manchester et al. 2005, 2016). Pulsars are far more numerous and have substantially weaker magnetic fields than active magnetars, typically in the range 10^{11}–10^{13} G. The catalogue provides best estimate distances, inferred from parallaxes, H I absorption, globular cluster associations, nebular lines, and stellar companions. Otherwise, the dispersion measure is used to infer a distance, in this case using the Yao et al. (2017) electron density model. We note that the majority of the sample are reliant on this model for a distance estimate, and will therefore be concentrated into the high electron density spiral arms. This is less of an issue in the local disc, where other distance measurements are more prevalent.

Incompleteness is likely higher in this sample than the magnetars, as shown in Fig. 1. However, pulsars are sufficiently numerous that a cut can be placed at high luminosity, such that a large region is covered in a less biased way, with the exception of the known dearth of pulsars in the GC. This detection bias along central sightlines arises due to the high dispersion measure here (Rajwade, Lorimer & Anderson 2017). We will later demonstrate the effect this has by comparing pulsar fraction of light distributions that include and exclude the Galactic bulge region.

The chosen cut is 65 mJy kpc^2. This is the lowest cut that yields approximately constant numbers across the whole Galaxy (specifically, it yields numbers either side of the GC heliocentric distance that are consistent within Poisson uncertainties). To make the numbers exactly equal across both halves of the Galaxy requires a harsh cut, reducing the total to only a handful of sources. Our chosen cut-off is a compromise between sample size and completeness. We later vary this threshold to determine the impact on our fraction of light results. The $y < 8.3$ kpc half-Galaxy cut is applied *after* the luminosity threshold is applied to the whole catalogue.

2.3 Low-mass X-ray binaries

XRBs are systems containing an accreting black hole or neutron star; low-mass XRBs (LMXBs) have a donor star masses that are typically $\lesssim$2.5 M$_\odot$. Although still subject to luminosity–distance completeness issues, XRBs benefit from having a maximum theoretical luminosity (the Eddington luminosity) and therefore distances can be approximated from X-ray observations alone, in the absence of other indicators (Jonker & Nelemans 2004). We use the INTEGRAL (Winkler et al. 2003) sample of Sazonov et al. (2020), consisting of LMXBs detected by the hard X-ray sensitive telescope IBIS. Some distances in the catalogue are estimated from *Gaia* parallaxes of the optical counterpart, which may be introducing a local bias in the sample with measured distances.

Krivonos et al. (2017) show the distance contours at which X-ray sources of given luminosities can be detected in the INTEGRAL survey. The majority of the Galaxy is covered with high completeness down to hard X-ray luminosities of 2×10^{35} erg s^{-1}, which is the lower end of the LMXB luminosity distribution. The sensitivity map provided by Krivonos et al. (2017) shows that coverage is not uniform, as total survey time varies with Galactic longitude. However, the contours can be approximated as circular from a location that is ~3–5 kpc closer to the GC than the Sun (see fig. 2 of Krivonos et al. 2017). Since the 2×10^{35} erg s^{-1} limit is ~20 kpc away from this point in all directions, only the outskirts of the Galaxy are affected by survey biases, which should be of minimal impact. As the accretor type (i.e. neutron star or black hole) is often ambiguous, we do not attempt to separate them. The XRB populations in this paper therefore include a small contribution from black hole systems.

2.4 High-mass X-ray binaries

A review and catalogue of INTEGRAL-detected high-mass X-ray binaries (HMXBs) is presented by Kretschmar et al. (2019). HMXBs are typically neutron stars (although black hole systems also exist), accreting material from a $\gtrsim$5 M$_\odot$ companion. They are among the brightest X-ray sources in the Galaxy, as such the sample should have high completeness across the region being considered. As for the LMXBs, where available, distances are estimated from *Gaia DR2* parallaxes. The projected locations therefore reflect both actual HMXB locations and survey/catalogue biases (the impact of which will be quantified in Section 5). When a distance is uncertain and a range is given, we use the mean of the upper and lower estimates. As for the LMXBs, we do not separate black hole and neutron star systems.

2.5 Comparison to other Galactic population studies

We now discuss the broad spatial distributions of our final samples in the context of previous mapping efforts. Distributions in Galactic latitude b, longitude l, and radial offset r from GC are shown in Fig. 2. Also shown on the b and l panels are SFCs from Russeil (2003), and the hot luminous star catalogue of Zari et al. (2021), which is restricted to the local 3–4 kpc. Faucher-Giguère & Kaspi (2006) and Yusifov & Küçük (2004) studied the Galactic pulsars population and found similar b and l distributions to both the pulsar sample shown here and young stars/SFCs, as expected.

The LMXB study of Jonker & Nelemans (2004) produces a similar range in b (with the majority in the central 15 deg) and l (concentrated

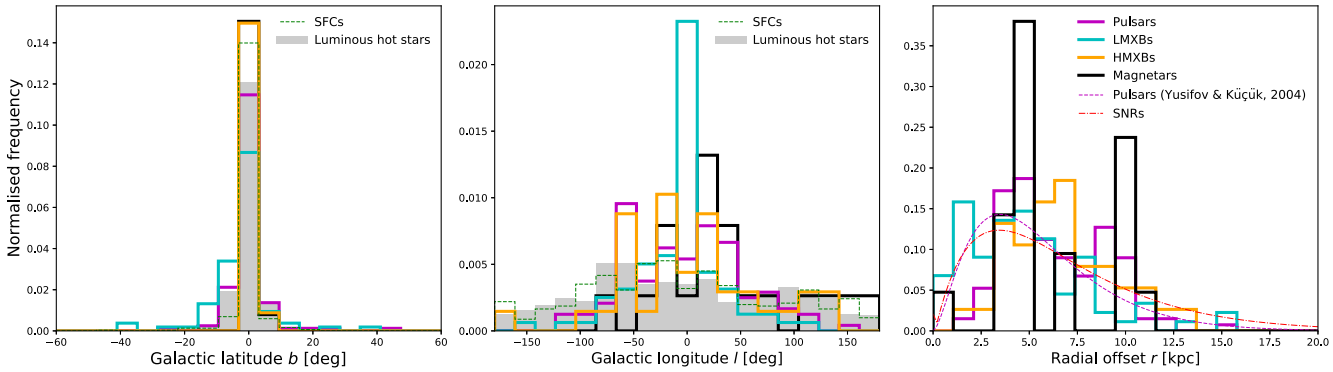

Figure 2. Normalized distributions in Galactic latitude, longitude, and radial offset for the four Galactic neutron star samples described in Section 2, with cuts applied. These are compared to SFCs (Russeil 2003), SNRs (Verberne & Vink 2021), hot luminous stars (Zari et al. 2021), and the pulsar distribution of Yusifov & Küçük (2004). The distributions of the neutron star samples are generally in good agreement with the previous works shown here, and others as discussed in the text. Perhaps the most prominent difference is the excess – particularly of magnetars – at 9–10 kpc, above the smooth Yusifov & Küçük (2004) and Verberne & Vink (2021) profiles, possibly associated with the Perseus arm.

in the 30 deg towards GC). Arnason et al. (2021) show that LMXBs do not correlate with spiral arm structure, this can be seen in Fig. 2 in their smooth l distribution compared to magnetars, pulsars, and HMXBs. A number of studies have noted HMXB correlations with spiral arms and SFCs (Bodaghee et al. 2007, 2012; Coleiro & Chaty 2013; Arnason et al. 2021), which can be seen here in l distributions of the HMXB (and magnetar and pulsar) samples, where overdensities correspond to tangents to the spiral arms. These samples also have slightly increased numbers towards central longitudes compared to SFCs and hot stars, which may be an artefact of X-ray and radio surveys spending more time in this region.

On the right-hand panel of Fig. 2, we show the Galactocentric radial offset distribution for the four neutron star samples, plus the pulsar distribution of Yusifov & Küçük (2004) and the SNR distribution inferred by Verberne & Vink (2021). Our Manchester et al. (2005) derived pulsar sample appears shifted to higher offsets by $\sim$1 kpc compared to Yusifov & Küçük (2004), similar to the simulated distribution of Faucher-Giguère & Kaspi (2006). The SNR distribution, which should in principle trace the locations of young neutron stars, is similarly more centrally concentrated. However, for the magnetars ($N = 20$) and HMXBs ($N = 36$) in particular, the samples are small enough that Poisson uncertainties may be producing noticeable differences between these distributions. The largest discrepancy is the excess of magnetars at 9–10 kpc, over the smooth Yusifov & Küçük (2004) and Verberne & Vink (2021) curves. While this may partly be due to low number statistics, an overdensity here could also be due to the Perseus arm. Nevertheless, the final half-Galaxy samples summarized in Table 1 broadly follow the expected trends when compared to previous studies of various Galactic populations.

3 BUILDING A FACE-ON MILKY WAY IMAGE

In this section, we construct an image of the Milky Way in two photometric bands, on which the four neutron star populations can be placed, and measured in the same way as extragalactic transients on their hosts. As in the previous section, we restrict the mapping to $y < 8.3$ kpc. This is to match the spatial extent of the neutron star samples, and because the extrapolation of the local spiral arm structure to the far side of the disc is highly uncertain. We now describe the construction of the half-Galaxy image from three core components – the spiral arms, a smooth underlying disc, and the bulge/bar.

3.1 Spiral arms

In order to map out where ongoing star formation is occurring in the Milky Way, we follow the approach of Reid et al. (2019), who use water and methanol masers to trace out the spiral arm structure in 3D. Masers are uniquely suited to this, as they are numerous, bright, and their detection is relatively unaffected by foreground absorption. In brief, Reid et al. (2016, 2019) use parallax measurements of various maser sources [SFCs, young stellar objects (YSOs), asymptotic giant branch stars and others; Valdettaro et al. 2001; Pestalozzi, Minier & Booth 2005; Green et al. 2017; Anderson et al. 2012; Urquhart et al. 2014] to infer the spiral arm positions and parameters locally, including pitch angle and tightness. The arms are then extrapolated around the entire Galaxy. Because radio observations of masers yield radial velocities, which can be converted into a local standard of rest velocity $V_{\rm LSR}$, the velocity structure of the Galaxy can be mapped out to distances beyond where parallaxes can be measured. They develop a Bayesian code, with the estimated arm positions as a prior, that can infer the likeliest distance given only a Galactic latitude, longitude, and LSR velocity. The warp of the disc is accounted for in the model (see Reid et al. 2016). The code includes a prior (0–1) for whether the source is near or far, as the $V_{\rm LSR}$ measurements contain a distance degeneracy for sightlines along a circular path.

We follow the same methodology as Reid et al. (2019) but restrict ourselves to the Red MSX catalogue of Urquhart et al. (2014, see also Lumsden et al. 2013). Where a near or far distance is favoured in the Urquhart et al. (2014) catalogue, we use $P_{\rm far} = 0$ or 1 as appropriate, otherwise $P_{\rm far} = 0.5$. Although less Galactic structure is mapped out by using a single input catalogue, the luminosity distribution is well understood, as is the incompleteness as a function of distance. Limiting ourselves to a single, well-understood catalogue also avoids double counting SFCs or single sources that appear in multiple maser catalogues. We further limit the sample to H II regions and YSOs, in order to trace out star formation specifically. The resultant star-forming region catalogue comprises 1644 sources.

Taking the 1644 H II region and YSO masers of Urquhart et al. (2014), we run the Bayesian distance FORTRAN code of Reid et al. (2019) and obtain a Milky Way spiral arm map. Beyond 3 kpc, the completeness of the input catalogues drops off as a function of distance from the Solar system (inverse square law) and Galactocentric radius (mainly due to source confusion towards the GC). We want to correct for this, so that the following three requirements are satisfied:

(i) The mean distance from each H II region/YSO maser to the next nearest neighbouring maser as a function of Galactocentric radius does not depend on Galactocentric azimuthal angle,
(ii) The mean number of masers within a fixed distance of each maser, again as a function of Galactocentric radius, does not depend on Galactocentric azimuthal angle,
(iii) The luminosity function of the masers is the same across the map.

To compensate for the high level of incompleteness at larger distances, we aim to match the density of sources in the local (∼3 kpc) neighbourhood according to the above metrics, across the (half) Galaxy.

We again follow the method of Reid et al. (2019). Artificial masers (sprinkles) are added at random x and y offsets from each of the 1644 *real* maser positions. The number of sprinkles added per real H II region/YSO maser varies as a function of distance from Earth and the Galactocentric radius. More random sprinkles are added at larger distances, and the width of the Gaussian used to determine the random x and y offsetss from the existing maser positions increases with Galactocentric radius (to reflect the widening spiral arm width). This process is described by the following. The number of sprinkles added for each of the 1644 masers is given by

$$N_{\rm sprinkle} = \left(\frac{D}{3{\rm kpc}}\right)^2 - N_{\rm corr} \quad (1)$$

at distances greater than 3 kpc. Below this, no sprinkles are added. The maximum number added is 10, and the minimum 1. $N_{\rm corr}$ is a correction to the form given by Reid et al. (2019), which is necessary given our smaller input catalogue size. The $N_{\rm sprinkle}$ sources are added following Gaussians in x and y. The standard deviation in each is given by

$$\sigma_{xy} = \frac{336 + 36(R_g - 8.15)}{W_{\rm corr}}, \quad (2)$$

where $W_{\rm corr}$ is a correction we have added, again needed in order to tune the random sprinkling to match the local 3 kpc density of points. In Reid et al. (2019), with their large input catalogue, $N_{\rm corr} = 0$ and $W_{\rm corr} = 1$.

A final issue is that there is a dearth of sources in a cone of around ∼30 deg towards the GC. On our side of the GC, this is corrected for by fitting a parabola to join the gap in the arms and sprinkling points along these curves so that their spatial density is comparable to the arms either side of the gap. No correction is made to the far side of the disc, as we only consider the half-Galaxy at $y < 8.3$ kpc going forwards.

In order to tune the incompleteness corrections described by equations (1) and (2), so that the first two bullet-point criteria above are met, we vary $N_{\rm corr}$ and $W_{\rm corr}$. The Galaxy is split into three regions: sources within 3 kpc, those in the helicoentric distance range 3–8 kpc, and those beyond 8 kpc. In Fig. 3, the target radial profiles are shown in black, representing the maser distribution in the local 3 kpc. We aim to find $N_{\rm corr}$ and $W_{\rm corr}$ values such that, when the artificial maser sprinkles are added, the 3–8 and >8 kpc profiles match those at <3 kpc. This will correct for incompleteness, so that it is at least

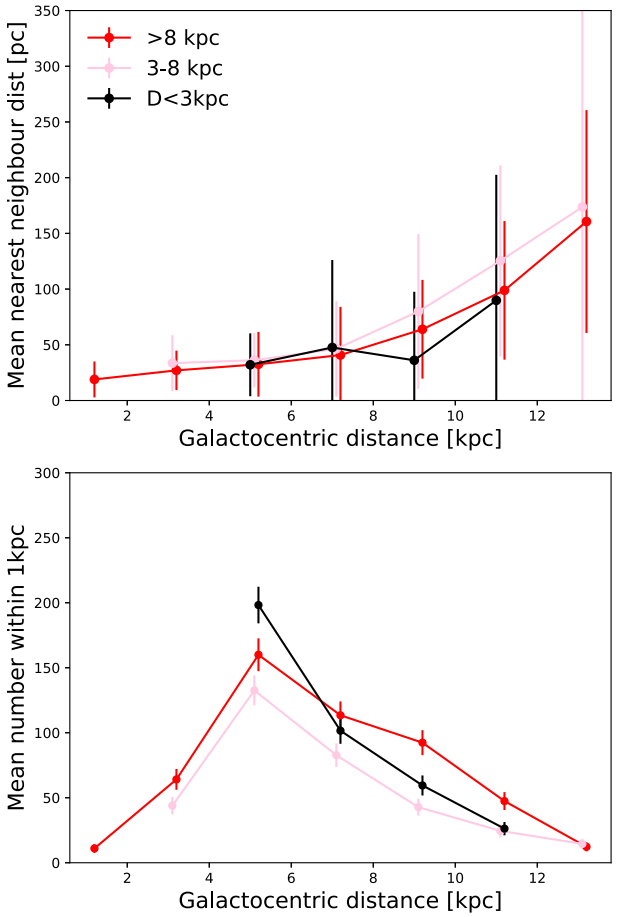

Figure 3. Upper panel: The mean distance to the nearest neighbouring maser, following the method of Reid et al. (2019) as described in the text. The three heliocentric distance ranges have approximately equal maser density as a function of Galactocentric distance. Lower panel: The mean number of masers within 1 kpc of each maser, again as a function of radial distance from GC. The arm width and $N_{\rm sprinkle}$ functions used to add artificial masers are given in equations (1) and (2).

uniform across the half-Galaxy region in consideration. We find that the default $N_{\rm corr} = 0$ and $W_{\rm corr} = 1$ values from Reid et al. (2019) provide a poor agreement between local sources and the rest of the Galaxy, unsurprising given our smaller input catalogue. Sampling values in the range 0–8, $N_{\rm corr} = 6$, and $W_{\rm corr} = 5$ provide the best match in terms of χ^2 between the local and more distant regions. The result is shown in Fig. 3.

Each sprinkle is also assigned a bolometric luminosity. Inside 3 kpc, the Urquhart et al. (2014) catalogue is complete down to bolometric luminosities of 1000 $L_\odot$. Therefore, outside 3 kpc, the randomly sprinkled points are assigned a luminosity drawn randomly from the distribution below the completeness limit at that distance. In this way, the luminosity function is approximately constant across the half-Galaxy map, complete down to 1000 $L_\odot$ everywhere.

The resultant maser map is shown in the left-hand panel of Fig. 4 (and can also been seen in the final image, see Fig. 5). To compare the arm positions to other Milky Way spiral arm maps, references include Vallée (2002, 2008), Russeil (2003), Faucher-Giguère & Kaspi (2006), and Churchwell et al. (2009), in addition to more local mapping efforts using *Gaia* (e.g. Castro-Ginard et al. 2021; Zari et al. 2021) and electron density models (e.g. Cordes & Lazio 2002).

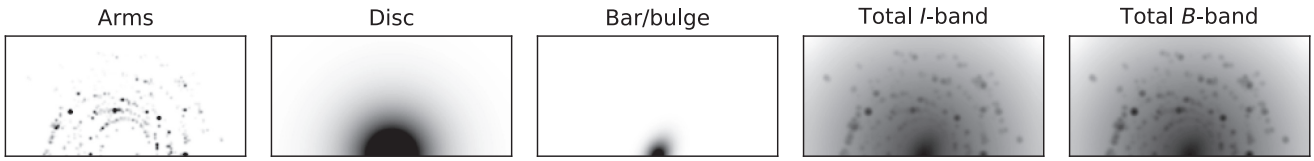

Figure 4. The three Galaxy components used, and their combination (with appropriate scaling) to produce the *I*- and *B*-band images. The spiral arm locations are derived from YSO and H II region masers in the Urquhart et al. (2014) catalogue, assigned a distance using the Reid et al. (2019) distance calculator. The disc is an exponential with scale length 2.6 kpc, and the bulge is a Sérsic profile convolved with the bar profile of Grady, Belokurov & Evans (2020), at an angle of 27 deg to the Sun–GC line.

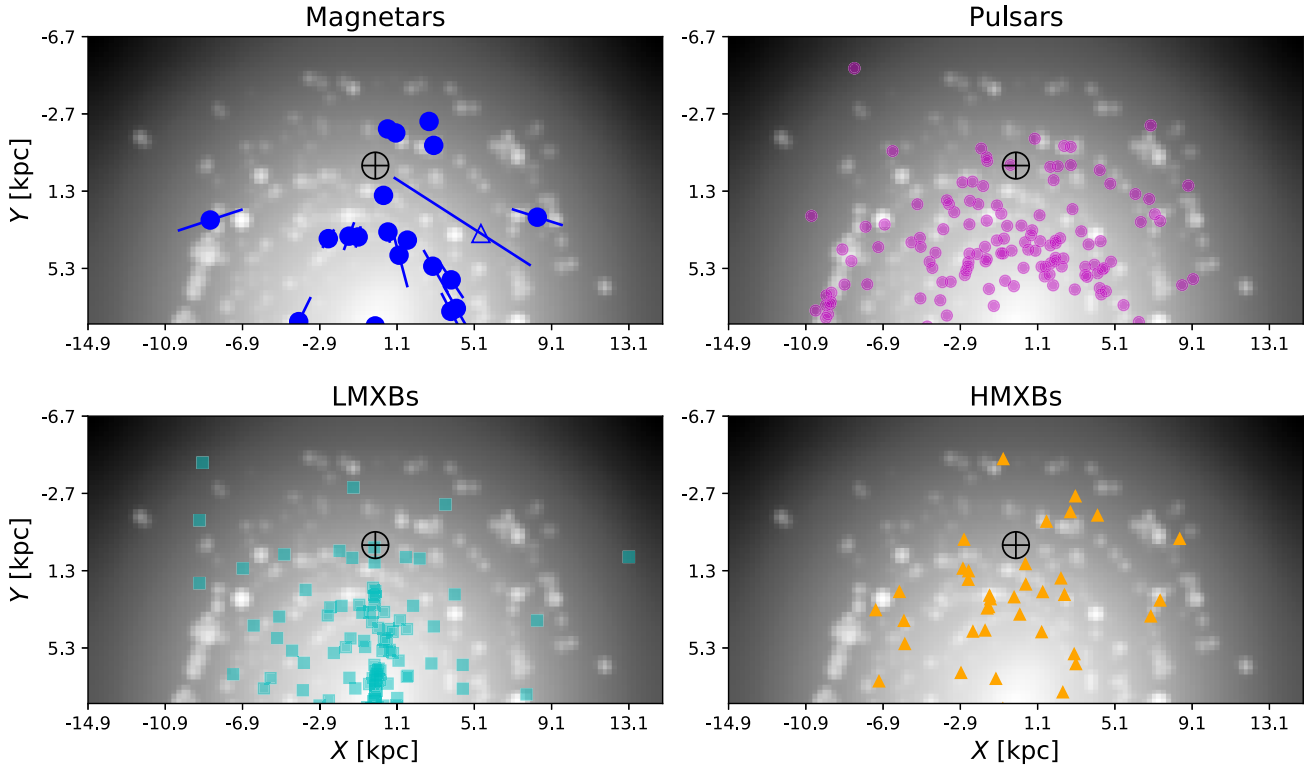

Figure 5. The Milky Way map overlaid with magnetars positions (top left, blue dots with distance uncertainties indicated; Olausen & Kaspi 2014), pulsars (top right, magenta dots; Manchester et al. 2005), LMXBs (bottom left, cyan squares; Sazonov et al. 2020), and HMXBs (bottom right, orange triangles; Kretschmar et al. 2019). The Solar system is located at (0,0), and GC at (0,8.3). The FRB source SGR 1935+2154 is indicated in the magnetar panel by a triangle. Only the half-Galaxy region shown is used for measurements throughout, to limit the impact of heliocentric distance uncertainties and detection biases.

3.2 The disc, bulge, and bar

In addition to the arms, the Milky Way has a disc (in which the arms are embedded) and a central bulge/bar. Our basic model follows Widrow, Pym & Dubinski (2008) and Bland-Hawthorn & Gerhard (2016). We model the disc with an exponential profile, adopting a scale length of $R_{\rm d} = 2.6$ kpc. This value is based on the range in the literature, and is around the mean of thin disc (which dominates the disc stellar content) values. The bulge is modelled as a Sérsic profile with index $n = 1.32$ and half-light radius $R_{\rm d} = 0.64$ kpc (Widrow et al. 2008). To account for the bar, this is convolved with the bar profile as mapped by Mira variables in *Gaia* (Grady et al. 2020). The angle between the Sun–GC line and bar semimajor axis is taken to be 27 deg (e.g. Binney, Gerhard & Spergel 1997; Bland-Hawthorn & Gerhard 2016).

3.3 Weighting the components

The three components – a smooth disc, embedded arms, and bulge/bar – now need weighting to represent their respective contributions to the total luminosity of the Milky Way. This will also be wavelength dependent.

As a starting point, we take the bulge and disc luminosities of Flynn et al. (2006), where the disc includes the arms. The *I*-band bulge and disc luminosities are 10^{10} and 3×10^{10} $L_\odot$, respectively.

The procedure described in Section 3.1 means that we have a value for the total bolometric luminosity of the masers above the 1000 $L_\odot$ limit, 1.78×10^8 $L_\odot$. This is twice the Urquhart et al. (2014) estimate for the total contribution of high-mass embedded star formation to the Galactic luminosity (due to differences in incompleteness corrections). However, for our purposes we are only interested in the

spiral arm locations, and the *relative* flux contributions of the galaxy components.

To determine what fraction of the disc light should arise from the spiral arms versus the smooth underlying exponential, we adopt an arm strength of 0.15 in the *I* band, typical for Milky Way mass galaxies (e.g. Díaz-García et al. 2019; Yu & Ho 2020). Arm strength is defined as the ratio of disc surface density arising from the $m = 2$ spatial Fourier component, versus the $m = 0$ component (Seigar & James 1998). It therefore quantifies the proportion of disc light arising from short spatial scales (i.e. the spiral arm structure). Arm strength varies in different bands, as the spiral arms are usually slightly bluer than the interarm regions – for *I*-band strengths of 0.15, typical *B*-band strengths are ∼0.2, values which we use going forward (Yu et al. 2018).

We now assume that *I*-band luminosity of the maser-associated H II regions is proportional to their maser-inferred bolometric luminosity. If the *I*-band arm strength is 0.15, the *I*-band exponential disc must have a luminosity ∼5.5 times that of the arms. The *I*-band bulge/bar luminosity is then one-third of the disc + arm total (as the Flynn et al. 2006 disc value includes spiral arms). The constants in the exponential disc and Sérsic profiles are scaled to reflect these respective contributions to the *I*-band light.

We now have an *I*-band image with the components appropriately scaled. However, the *I* band is a better tracer of stellar mass than star formation. To obtain a bluer version of the image, we use the $B - I$ colours of Licquia et al. (2015), who estimate a total integrated Galaxy colour – including dust – of 1.77. Bland-Hawthorn & Gerhard (2016) obtain an alternative value of 1.85 ± 0.1, but this is consistent with Licquia et al. (2015). Note that all *B* and *I* magnitudes and colours quoted in this paper are in the Vega system but they are converted to AB magnitudes to perform any calculations.

We now need the $B - I$ colour of either the disc or bulge in order to determine the *B*-band luminosities of all three components. Flynn et al. (2006) provide a local disc $B - I$ colour of 1.48, but this has been corrected for dust and is therefore artificially blue. We instead use the 'as observed' (not dust-corrected) Milky Way colour estimates of Licquia et al. (2015), which are based extragalactic analogues chosen for their mass and SFR similarity with the Milky Way. Within these analogues they identify a bulge-dominated subsample, which we use to estimate the Milky Way bulge colour. This has a mean *B*-band mass-to-light ratio (MLR) of 4.1. We also use their global MLR estimates in *I* and *B* of 1.29 and 1.89, and a bulge-to-total mass ratio of 0.3 (Bland-Hawthorn & Gerhard 2016). Taking the *I*-band component luminosities from Flynn et al. (2006), this implies a bulge/bar $B - I$ of 2.41.

We now have a bulge/bar $B - I$ of 2.41, a global $B - I$ of 1.77, and *I*-band luminosities for the total Galaxy and the components. We can therefore infer the colour of the final component (disc including arms) – 1.62 – and hence we have the luminosities of all three components in each band. This disc colour is bluer than the total integrated colour as expected, and 0.14 redder than the Flynn et al. (2006) dust-corrected value for the local disc.

3.4 The final Milky Way image

The construction of the final Galaxy image is shown in Fig. 4, in both bands. These images have a pixel scale of 250 pc per pix, and we have applied a Gaussian blur with a full width at half-maximum (FWHM) of 2 pixels to simulate *Hubble Space Telescope*, (*HST*) quality imaging (∼0.05 arcsec pix^{-1}). The masers are treated as point sources, and their luminosity is assigned to whichever pixel they fall under. In reality they are not point sources, but this unlikely to be a significant issue, as the majority of star-forming regions have radii <250 pc, and almost all <500 pc (Wisnioski et al. 2012). This effect is further diminished as they tend to have approximately Gaussian density profiles, so that the light contributed to neighbouring pixels will not usually be a significant fraction of the total star-forming region luminosity. The final *B*- and *I*-band images are similar, as the three input components have the same profiles, but the different scaling of these components with respect to each other means that there are differences (e.g. the light is more centrally concentrated in the *I*-band image). The final half-Galaxy *B*- and *I*-band images are available in fits format at https://github.com/achrimes2/MW-NS-Flight.

3.5 Placing Galactic neutron stars on the image

The final neutron star samples compiled in Section 2 are now placed on the half-Galaxy image constructed in Fig. 4. Their positions have been computed from the Galactic latitude, longitude, and given distance, correcting for a Solar system height above the Galactic plane of 15 pc (Olausen & Kaspi 2014, although this is negligible for our purposes). Their positions on the *B*-band image are shown in Fig. 5. The selected magnetars, bright pulsars, INTEGRAL LMXBs, and HMXBs are shown as blue circles, magenta circles, cyan squares, and orange triangles, respectively.

4 OFFSETS AND ENCLOSED FLUXES

4.1 Offsets

Having selected our neutron star samples in Section 2, and constructed Milky Way model in Section 3, we now move on to measuring how neutron stars are distributed with respect to Galactic structures and light. We start with their offsets from GC.

We now look at the offsets of the neutron stars from the GC. Our offsets measurements are 2D projections of the 3D distance from GC. Both offsets δr and host-normalized offsets $\delta r/r_e$ are shown in the upper panels of Fig. 6, where r_e is the half-light radius. For our Milky Way image, $r_e = 2.37$ kpc in the *B* band and 2.22 kpc in the *I* band. In principle, normalizing by the half-light radius should make comparisons between galaxies of different physical sizes fairer.

The four Galactic samples are compared to extragalactic transient offsets distributions, shown in the lower two panels of Fig. 6. The comparison data are from Mannings et al. (2021, FRBs), Blanchard, Berger & Fong (2016); Lyman et al. (2017, long GRBs), Fong et al. (2013, short GRBs), Uddin et al. (2020, type Ia SNe), Kelly & Kirshner (2012); Schulze et al. (2021, CCSNe), Lunnan et al. (2015); Schulze et al. (2021, SLSNe), and Lunnan et al. (2017); De et al. (2020b, Ca-rich SNe). We have also added the M81 repeater to the FRB distribution (Bhardwaj et al. 2021). The results of Anderson-Darling (AD) tests between the magnetar/pulsar/XRB offsets and the comparison samples are listed in Table 2. Results that do not round up to 0.01 are simply listed as 0.00. The maximum value is 0.25, as outputs are capped at this value by the SCIPY Anderson function.

Across the four Galactic samples, FRBs most frequently have a *p*-value >0.05. Only the *I*-band normalized results are shown in Fig. 6, using the *B*-band half-light radius results in slightly less offset distributions (we refer the reader to Appendix A, where the full magnetar results are listed in Table A1, and access to the data for the other samples is described).

To quantify the uncertainty on the magnetar distribution, we take the maximum and minimum offsets possible along the line of sight,

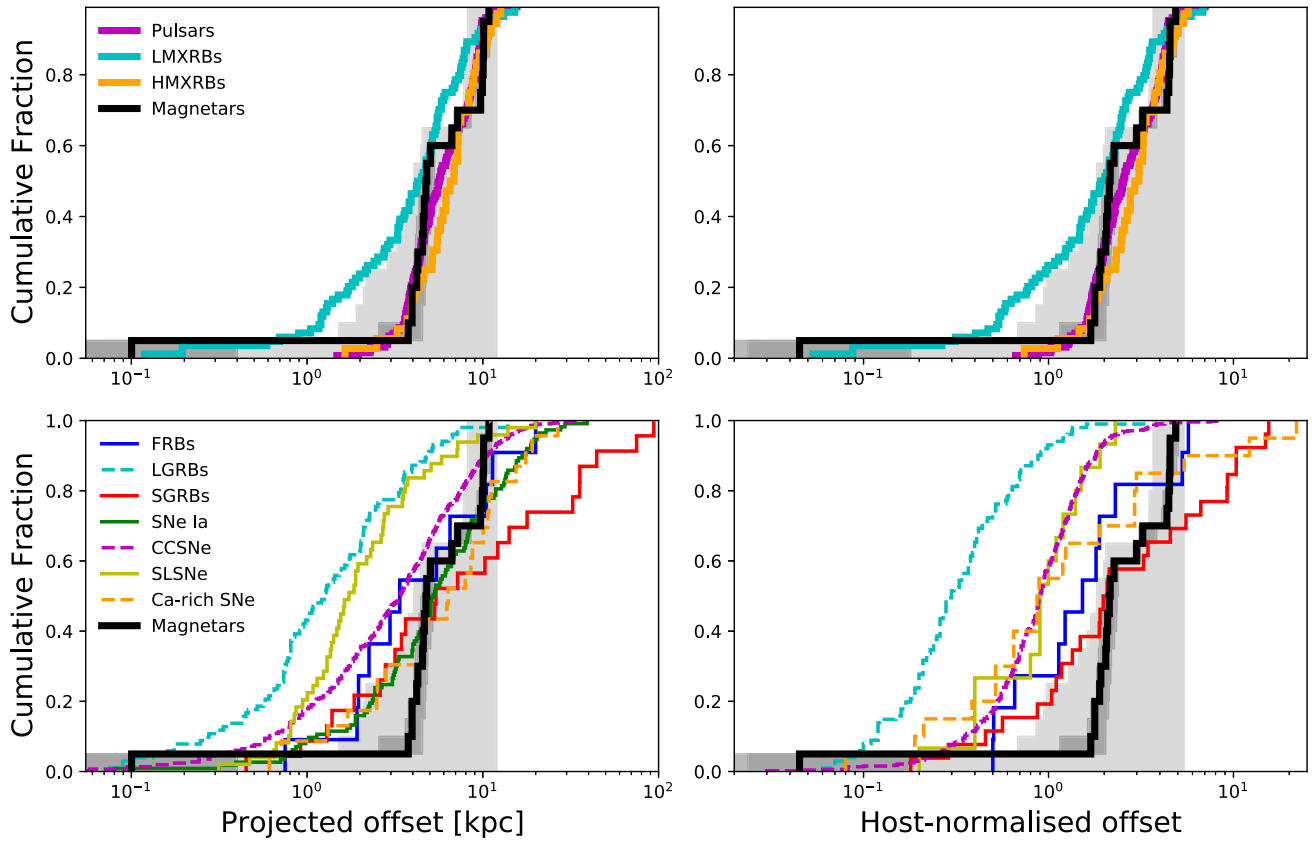

Figure 6. Projected (left) and host normalized (right) offsets for Milky Way magnetars, compared to other Galactic neutron star systems (top row) and the offsets of extragalactic transients on their hosts (bottom row, shown separately for clarity). FRB 20200120E has been added to the FRB offset data set, assuming association with M81 (Bhardwaj et al. 2021). The light grey shaded region is bounded by the extreme upper and lower distributions for the magnetars, assuming the maximum and minimum offsets possible along that line of sight (and that the magnetar lies 'in' the Galaxy, at $\delta r < 12$ kpc). The narrower dark grey shading indicates the maximum and minimum allowed within the quoted magnetar distance uncertainties. A 15 per cent error is used where one is not available. The *I*-band host-normalized offset is shown (with half-light radius $r_h = 2.22$ kpc), similar results are obtained using the *B* band r_h of 2.37 kpc (see Table A1 of Appendix A).

assuming that the magnetars lie 'inside' the Galaxy (i.e. <12 kpc from GC). The region bounded by the minimum and maximum possible distributions is shaded light grey in Fig. 6. We also take the listed uncertainties, shading between the quoted upper and lower bounds produces the narrower dark grey band. Even if we consider the lowest offsets that the magnetars could possibly have along their sightlines, they cannot match the CCSN offset distribution.

Looking at Fig. 6, it is evident that the specific morphology of the Milky Way dictates the shape of the Galactic distributions. The choice of disc scale length has an impact of the normalized offsets, but literature estimates only vary by at most a factor of ∼1.5–2 (Bland-Hawthorn & Gerhard 2016). Much of the light is concentrated centrally in the bulge (in both bands), a predominantly older population where fewer young neutron stars reside. Consequently, the LMXBs (known to be a older population) appear distributed on the Milky Way's *I*-band light in a similar way to supernovae on their hosts, although this does not imply a connection. Likewise, the younger pulsars, HMXBs, and magnetars are more offset than the short delay time extragalatic transients. This arises because we are dealing with a single Galaxy: in the extragalactic samples, the range of host morphologies, sizes, and viewing angles removes any such trends.

There may also be issues related to faint, halo light that is not detected in extragalactic samples (Perets & Beniamini 2021), and other Galaxy-specific morphological effects that influence the offsets and flux profile, such as the specific arm locations. For example, the Galactic ring of star formation at 3–5 kpc has a high density of magnetars, relative to other arm structures. This is reflected as a dearth of objects at <3 kpc and a rapid climb in the cumulative distribution at 3–5 kpc. Interestingly, magnetar locations appear to favour this inner, nuclear ring, over spiral arms further out. This does not appear to be a distance-sensitivity effect as similarly bright arms at comparable heliocentric distances still have fewer magnetars. This may be suggestive of other factors playing a role in their production, beyond a high SFR (such as metallicity or initial mass function variations) and warrants further investigation.

4.2 Enclosed fluxes

Another way to measure how the neutron stars relate to light is to measure the fraction of the total Galactic flux enclosed at their radial distance. We calculate this for the magnetar, pulsar, and XRB samples, comparing to supernova (Anderson & James 2009; Anderson et al. 2015) and FRB distributions (Mannings et al. 2021) in Fig. 7. The grey shaded regions are the magnetar uncertainties, calculated in the same way as for the offsets. We again restrict the samples and pixels to $y < 8.3$ kpc, and measure the fraction of flux enclosed in the semicircle produced.

Table 2. Offset and host-normalized offset AD test results, for the comparisons made in Fig. 6. Top: offsets, middle: *B*-band host-normalized offset (the comparison data are also normalized in a UV/blue band where available), bottom: *I*-band host-normalized offset (comparison data normalized in an *r* or *I* band). *p*-values of 0.05 or greater, indicating statistical consistency, are highlighted in bold and have a grey background. None of the Galactic populations are consistent with LGRBs, SLSNe, or CCSNe according to this measure. Note that host-normalized data for SNe Ia are not available.

	LGRB	SLSN	CCSNe	FRB	SNe Ia	SGRB
Offset						
Magnetars	0.00	0.00	0.00	**0.07**	**0.17**	0.00
HMXRBs	0.00	0.00	0.00	0.02	0.02	0.00
Pulsars	0.00	0.00	0.00	0.00	0.00	0.00
LMXRBs	0.00	0.00	0.04	**0.25**	0.01	0.00
B-band normed						
Magnetars	0.00	0.00	0.00	0.04	n/a	**0.08**
HMXRBs	0.00	0.00	0.00	0.00	n/a	0.01
Pulsars	0.00	0.00	0.00	0.00	n/a	0.00
LMXRBs	0.00	0.00	0.00	**0.25**	n/a	0.02
I-band normed						
Magnetars	0.00	0.00	0.00	0.02	n/a	**0.06**
HMXRBs	0.00	0.00	0.00	0.00	n/a	0.01
Pulsars	0.00	0.00	0.00	0.00	n/a	0.00
LMXRBs	0.00	0.00	0.00	**0.25**	n/a	0.03

AD-test results are given in Table 3. FRBs are the transient most often consistent with the various neutron star populations. The enclosed flux measurements, like the offsets, are biased by the specific morphology of the Milky Way, specifically because the neutron star distributions are being drawn from just one Galaxy. To disentangle these effects, we now look at the fraction of light statistic, which operates on a pixel-by-pixel basis and can be restricted to subregions within the Galaxy.

5 FRACTION OF LIGHT

We now turn to the fraction of light ($F_{\rm light}$; Fruchter et al. 2006) statistic. The $F_{\rm light}$ distribution is calculated by ranking host-associated pixels by brightness, and assigning each their value in the cumulative sum, normalized by the total (half) galaxy cumulative flux. The brightest pixel therefore has the value 1. Transients that arise from the light in an unbiased way produce an $F_{\rm light}$ cumulative distribution that follows a 1:1 line, those that are concentrated on brighter regions have a distribution below the 1:1 line, and those are that offset or avoid bright regions lie above this line. UV/blue bands are assumed to trace young stars and thus star formation, whereas IR/red bands better trace stellar mass.

The fraction of light method has the benefit of being less dependent on host morphology. For example, if a transient occurs on a bright star-forming region, but at a large offset from the host centre, both the offset and enclosed flux measurements will indicate a low likelihood of association with star formation/stellar mass (depending on the wavelength). The $F_{\rm light}$ value, however, will assign the proportionate ranking in the distribution of host pixels, ranking it highly, and correctly identifying a close association. It is also possible to restrict the region considered, for example, if we want to look solely at the disc (Lyman et al. 2017). This enables use to probe how transients (and in our case neutron stars) trace light in different stellar populations.

Because $F_{\rm light}$ relies on pixel values, the choice of spatial resolution is important. The adopted resolution of 250 pc per pixel is broadly typical of *HST* resolution for targets at cosmological ($z \sim 1$) distances.

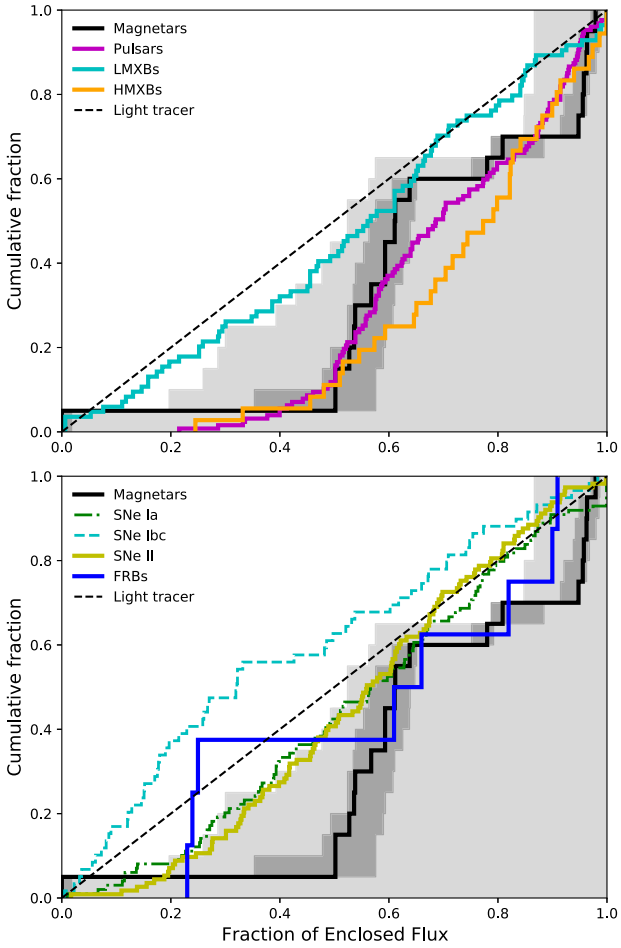

Figure 7. Top: Enclosed fluxes for the four Galactic samples. Bottom: The fraction of Milky Way flux (at $y < 8.3$ kpc) enclosed within the Galactocentric radius of the magnetars, the *I*-band version is used for a fairer comparison to the extragalactic samples. The maximum and minimum distributions possible for the magnetars are shaded in light grey, the same is shown in dark grey using their given distance uncertainties (or a 15 per cent error where one is not available).

Table 3. As for Table 2 but for enclosed fluxes. The distributions are shown in Fig. 7. Only the *I* band is used for a fair comparison to the extragalactic samples.

	Type Ia SNe	FRB	SNe II	SNe Ibc
Magnetars	0.04	**0.25**	0.02	0.00
HMXRBs	0.00	**0.11**	0.00	0.00
Pulsars	0.00	**0.07**	0.00	0.00
LMXRBs	**0.25**	**0.25**	**0.25**	0.01

5.1 Half-Galaxy results

We select all pixels at $y < 8.3$ kpc and within 12 kpc of the GC as being associated with the galaxy. Pixels outside this semicircular region are assigned $F_{\rm light} = 0$. The pixels in the half-Galaxy are ranked by their cumulative value and normalized. The pixel selection and $F_{\rm light}$ colour maps are shown in the upper panels of Fig. 8. In the lower

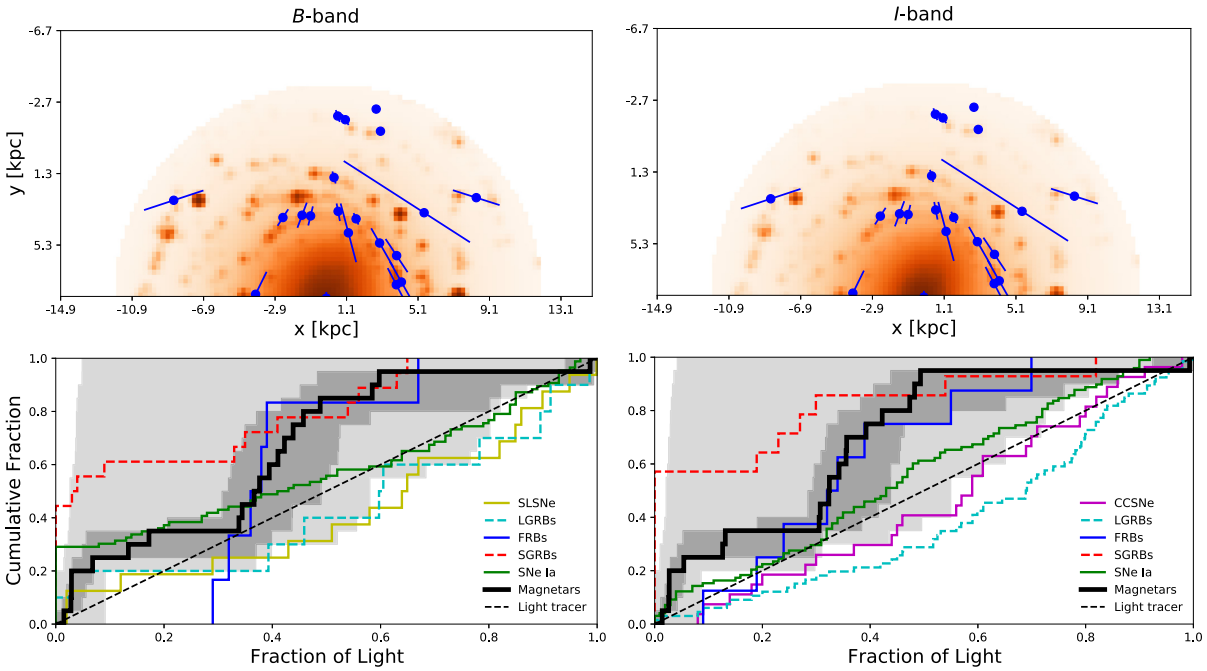

Figure 8. Upper panels: Half-Galaxy $F_{\rm light}$ colour maps with magnetar positions and uncertainties indicated (*B* band left, *I* band right). The 250 pc pixel^{-1} scale (with a 2 pixel FWHM) is broadly representative of *HST* spatial resolution for cosmological transients. Pixels within a 12 kpc Galactocentric radius are selected for calculating the $F_{\rm light}$ distributions. Lower panels: The corresponding fraction of light distributions for the magnetars (solid black lines). The light grey shaded regions represent the minimum and maximum distributions that arise from taking the minimum and maximum $F_{\rm light}$ values along the magnetar sightlines. This places a strong upper limit on how concentrated magnetars can be on the Galactic light. The darker grey bands use linear sampling between the McGill catalogue upper and lower distance estimates, taking the mean uncertainty of 15 per cent on a distance where a range is not provided. The distributions for various extragalactic transients on their host galaxies are also shown.

panels, magnetar $F_{\rm light}$ distributions are compared with extragalactic transients. The comparison data are from Mannings et al. (2021, FRBs), Blanchard et al. (2016); Lyman et al. (2017, LGRBs), Fong et al. (2013, SGRBs), Wang et al. (2013, type Ia SNe), Svensson et al. (2010, CCSNe), and Lunnan et al. (2015, SLSNe).

The light and dark grey uncertainty bands on the magnetar distributions are again derived from the maximum and minimum pixel values possible along the line of sight, and within the quoted distance ranges (or with a 15 per cent distance uncertainty if unavailable). Where an errorbar takes us past $y = 8.3$ kpc, or when calculating the full range of values along a sightline, we have to quantify the expected pixel values on the far side of the disc. To do this, we simply mirror the galaxy across $y = 8.3$ kpc, sampling the mirrored values out to the appropriate distance (either the upper distance estimate, or the 'edge' of the Galaxy). This should give a reasonable estimate of the range of pixel values expected for sightlines beyond $y = 8.3$ kpc, assuming the Galaxy is approximately symmetric on large scales.

The dark grey uncertainty band is somewhat larger here than for the offsets or enclosed fluxes. This is because we are now dealing with pixel values, which can have far more variation along the same line of sight than offsets (no dependence on pixel values) or enclosed fluxes (summing pixel values within a radius). We note that, because the quoted uncertainties are typically not formally quantified, we have simply shaded between the upper and lower heliocentric distances (i.e. assuming constant probability density in this range). In reality, the probability density closer to the assumed magnetar distances is likely greater than at the edges of these ranges.

Table 4. As for Tables 2 and 3, but for half-Galaxy *B* band (top four rows) and *I* band (bottom four rows) $F_{\rm light}$ comparisons, as shown in Figs 8, B1–B3.

	LGRB	SLSN	FRB	SN Ia	SGRB
Magnetars	0.02	0.01	**0.25**	0.01	0.01
HMXRBs	0.01	0.00	**0.11**	0.00	0.00
Pulsars	0.00	0.00	**0.21**	0.00	0.00
LMXRBs	**0.25**	**0.20**	**0.25**	0.00	0.00
	LGRB	CCSNe	FRB	SN Ia	SGRB
Magnetars	0.00	0.00	**0.25**	0.03	0.00
HMXRBs	0.00	0.00	**0.25**	0.00	0.00
Pulsars	0.00	0.00	**0.25**	0.00	0.00
LMXRBs	0.00	**0.10**	**0.25**	**0.25**	0.00

The uncertainties are slightly larger in the *B* band (this can be seen in Fig. 8), because the arms contribute a higher fraction of the total flux. Random variations in location due to distance uncertainties therefore sample a wider range of pixel values along a given line of sight, providing a wider range of possible distributions. Based solely on the range possible along a line of sight, it is possible that many magnetars actually lie on highly ranked pixels and are not inconsistent with CCSNe or even SLSNe. However, the LGRB distribution cannot be reached, independent of the heliocentric distances assumed.

AD tests between the magnetars/pulsars/XRBs and extragalactic transients are listed in Table 4. The equivalent figures for the pulsars and XRBs are available in Figs B1–B3 of Appendix B. Across the four Galactic samples, as we found for the offset and enclosed flux

measurements, FRBs fail to reject the null hypothesis that they are drawn from the same distribution as Galactic neutron stars the most often. SGRBs are the least consistent with Galactic neutron star populations (SGRBs are much less concentrated on the light).

The choice of pixel selection radius (12 kpc) has only a small impact on the resultant $F_{\rm light}$ values. For the interested reader, we have made PYTHON scripts and notebooks available that generate a similar $F_{\rm light}$ figure, given user defined input parameters.[3]

5.2 Local region results

In Sections 2 and 3, it was noted that sample completeness is higher, and distance estimates more reliable, in the local disc (within 3–5 kpc of our location). This is because trigonometric parallax measurements are possible in this region (both for the neutron stars and the masers), and survey sensitivities are less of a issue. There are also other biases, such as an absence of pulsars around the GC due to the high dispersion measures here (Rajwade et al. 2017, and see Fig. 5). Furthermore, using the half-Galaxy map mixes the older population of the bulge and the younger, higher SFR disc. In summary, our half-Galaxy comparisons to extragalactic samples may be suffering from biases that have not been fully corrected.

In order to quantify these effects on our results, we present $F_{\rm light}$ AD-test results for the local 4 kpc region versus extragalactic transient samples. In this region, completeness should be higher and distance uncertainties lower, as a higher proportion of the sample (particularly XRBs) have parallax-based distance estimates. We select pixels and neutron stars within 4 kpc of the Sun and $<$12 kpc from GC, and recalculate the $F_{\rm light}$ distribution for this area only. The magnetar results are shown in Fig. 9, alongside the half-Galaxy results to demonstrate the difference. The corresponding pulsar and XRB distributions are again shown in Figs B1–B3 of Appendix B.

Restricting the $F_{\rm light}$ analysis to the local disc has a larger impact in the *I* band than the *B* band, but in both cases has shifted the magnetars/pulsars/XRBs closer towards being light-tracers. This makes sense in terms of the Galactic morphology: younger magnetars and HMXB systems avoid the older (but bright) bulge, so the inclusion of the bulge in $F_{\rm light}$ calculations pushes them away from being unbiased tracers. Similarly, LMXBs – which are concentrated in the bulge – are shifted the least by its exclusion from $F_{\rm light}$. This also explains why the shift between half-Galaxy and local results is greater in *I*, as the bulge contributes a higher proportion of the total light in that band.

Table 5 lists the local region AD-test results. The results are less clear compared to the half-Galaxy comparisons. FRBs are again a good match to Galactic neutron stars, and the significance of this is even more apparent when the *p*-values are considered (reaching the 0.25 cap 6/8 times). However, unlike the half-Galaxy case, LGRBs, SLSNe, CCSNe, and thermonuclear SNe are also consistent with several Galactic populations. Plausibly, the smaller Galactic sample sizes that result from restricting ourselves to $<$4 kpc reduces the power of the AD-test, making consistency with other samples harder to rule out.

5.3 Fraction of light uncertainties

Aside from the impact of the multicomponent nature of the Galaxy on these results, uncertainties in both neutron star distances and spiral arm structure also play a role in shaping the distributions. For example, it is possible that the neutron stars appear artificially less concentrated with respect to light due to distance uncertainties. This should preferentially scatter them away from their natal star-forming regions, assuming they were born in star-forming regions, given that interarm regions take up more volume than the arms. The local region results should address this somewhat – in addition to removing the effect of the Galactic bulge, parallax measurements are possible here (both in the optical for XRBs and radio for pulsars).

A reason to suspect that arm position inaccuracies are not a major issue is that the spiral arm model is derived directly from trigonometric parallax measurements of CO/H I emission in the local disc (Reid et al. 2016). CO/H I tracers have previously been demonstrated to better trace arm mid-points than masers (Vallée 2014) – we are simply populating the CO/H I derived spiral arm model with the masers. Furthermore, the images we construct have a spatial resolution of 250 pc pixel^{-1} and a point spread function to replicate *HST*-quality imaging, which is insufficient to resolve the offset between arm mid-points and typical CO/H I offsets of 100–200 pc (Vallée 2014). In the local few kiloparsecs the spiral arm tracer distances are directly measured, beyond this the arms are extrapolated, but throughout we have neglected the far side of the disc where this extrapolation would be particularly problematic.

While the local 4 kpc comparisons are inherently less affected by uncertainties, the full half-Galaxy results are still valuable, as many transients do occur in galaxies with mixed populations and multiple components. This is particularly notable for FRBs, whose host galaxies are varied and include several Milky Way-like spirals and barred spirals.

The other assumptions we have made about the Galactic structure and the colour of the different components also contribute uncertainty, such as the adopted arm widths, which may have been underestimated. Zari et al. (2021) show that young stars are only loosely concentrated in the spiral arms (Arnason et al. 2021, find a similar result for HMXBs). Widening the arms by changing equation (2) in Section 3 would tend to increase the association of Galactic neutron stars with light. This is because any distance uncertainty induced offsets from nearby bright pixels will be reduced. However, the pixel values would also decrease (there would be fewer masers per pixel).

Overall, specific Galaxy mapping choices appear to be less important than Galactic neutron star sample incompleteness and distance uncertainties. We refer the reader to the interactive tools at https://github.com/achrimes2/MW-NS-Flight, which can be used to vary the relative light contributions of the bulge/bar, disc, and arms, to visualize the impact on $F_{\rm light}$. The spatial resolution of the image can also be degraded below the 250 kpc per pixel level used in this paper.

6 DISCUSSION

6.1 Summary of results

Table 6 gives an overview of our results, in terms of the percentage of times that the different extragalactic transients agree at the 2σ level ($p > 0.05$) with Galactic neutron stars, as measured on the Milky Way face-on image. The comparisons considered are the Galactocentric offsets and host-normalized offsets in both bands, the *I*-band enclosed flux, the *B*- and *I*-band half-Galaxy $F_{\rm light}$, and the local 4 kpc *B*- and *I*-band $F_{\rm light}$. The total number of AD-tests made against each transient is counted across Tables 2–5.

It is clear from Table 6 that the distribution of Galactic neutron stars on the Milky Way best matches, of all of the transients,

[3] https://github.com/achrimes2/MW-NS-Flight

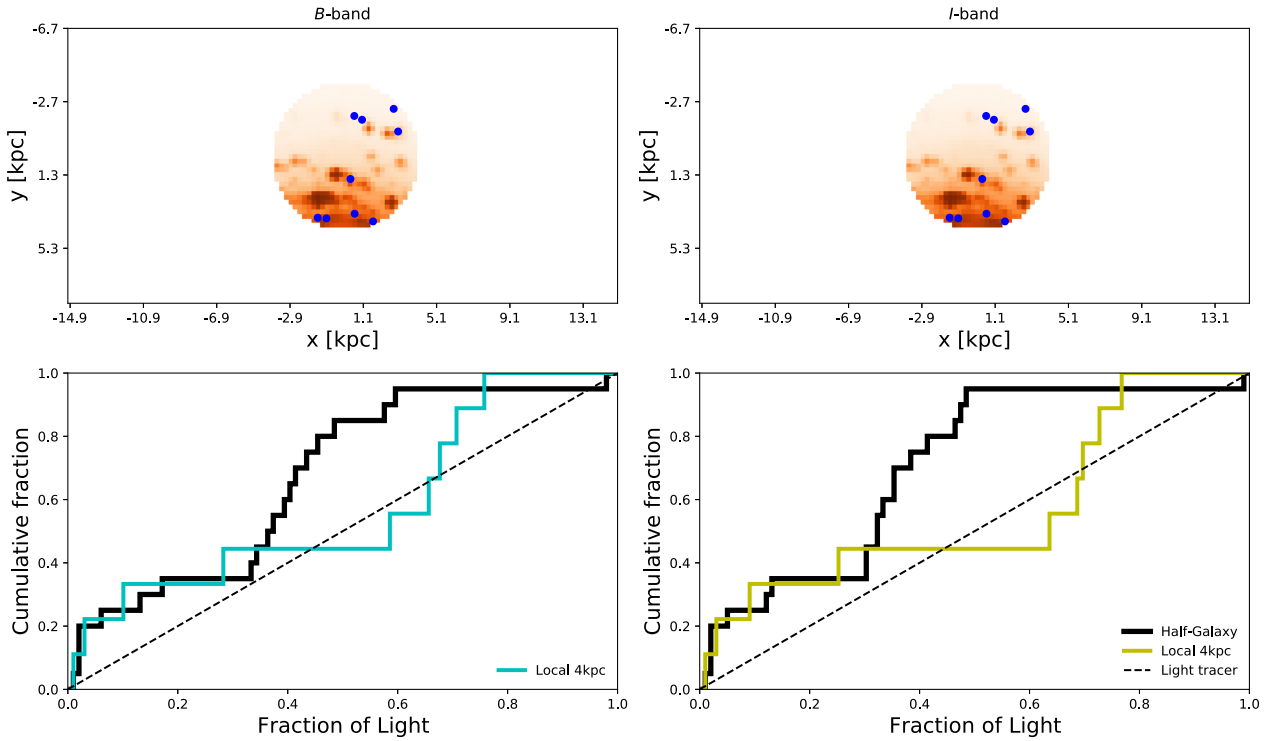

Figure 9. Exploring the effect of restricting the $F_{\rm light}$ analysis to the local disc (<4 kpc). This region has more accurate distance estimates for both the Galactic neutron stars and spiral-arm tracing masers. It also allows us to quantify the effect of the bulge on the distributions shown in Fig. 8, sampling a more uniform stellar population. Top: The pixel selection for $F_{\rm light}$ when a 4 kpc heliocentric distance restriction is applied. Bottom: Magnetar $F_{\rm light}$ distributions for the half-Galaxy as shown in Fig. 8, and the local region results in each band. Excluding the bulge pushes the distribution towards the 1:1 light-tracer line.

Table 5. $F_{\rm light}$ AD-test results for comparisons within the local 4 kpc only, as shown in Figs 9, B1–B3. Top four rows: *B* band, bottom four: *I* band.

	LGRB	SLSN	FRB	SN Ia	SGRB
Magnetars	**0.25**	**0.25**	**0.22**	**0.19**	0.00
HMXRBs	**0.25**	**0.24**	**0.25**	0.04	0.00
Pulsars	**0.07**	0.04	**0.25**	0.01	0.00
LMXRBs	**0.22**	**0.11**	**0.15**	0.02	0.00
	LGRB	CCSNe	FRB	SN Ia	SGRB
Magnetars	**0.09**	**0.23**	**0.25**	**0.25**	0.00
HMXRBs	**0.06**	**0.25**	**0.25**	**0.25**	0.00
Pulsars	0.00	**0.14**	**0.25**	**0.25**	0.00
LMXRBs	**0.13**	**0.25**	**0.19**	**0.25**	0.00

Table 6. For each extragalactic transient, the number of comparisons made to magnetar, pulsar, and XRB systems on the Milky Way is listed, along with the number and fraction of those tests which return at *p*-value >0.05. The results used to populate this table are listed in Tables 2 (offsets and host-normalized offsets in both bands), 3 (enclosed fluxes, *I*-band only), 4 (half-Galaxy $F_{\rm light}$), and 5 ($F_{\rm light}$ in the local 4 kpc). Overall, FRBs are clearly distributed on their hosts in a similar manner to neutron stars on the Milky Way, and are a better match than the other transients tested.

Transient	$N_{\rm AD\text{-}test} > 0.05$	$N_{\rm AD\text{-}test}$	Fraction >0.05
LGRB	8	28	0.29
SLSN	4	20	0.20
CCSNe	6	28	0.21
FRB	24	32	0.75
SNe Ia	8	24	0.33
SGRB	2	28	0.07

FRBs on their hosts. However, we are unable to clearly differentiate which class of neutron star is the best fit – within the FRB AD-tests, magnetars return $p > 0.05$ on six occasions, HMXBs/pulsars five times each, and LMXBs eight times.

Of the other extragalactic transients, SGRBs (known to be mergers involving at least one neutron star; Barthelmy et al. 2005; Fong et al. 2010; Church et al. 2011; Tunnicliffe et al. 2014; Abbott et al. 2017) are the worst match. SRGBs have extended offset distributions, due to the combination of natal kicks and long gravitation wave inspiral times. The implication is that, in the Milky Way, old, kicked systems are missing from our catalogues, possibly because they are distant and not bright emitters like magnetars, pulsars, or XRBs. Of the other samples, none stand out as being more or less consistent with the Galactic systems.

6.2 Implications for the neutron star–FRB connection

Initial FRB host population studies (Heintz et al. 2020; Mannings et al. 2021) led to differing interpretations over whether magnetar flares can explain all FRBs (Margalit et al. 2020; Safarzadeh et al. 2020; Bochenek, Ravi & Dong 2021). It is also unclear whether the identification of FRB-like flares from SGR 1935 (Bochenek et al. 2020; CHIME/FRB Collaboration 2020) definitively establishes a connection between magnetars and extragalactic FRBs (Bailes et al. 2021; Ridnaia et al. 2021; Tavani et al. 2021).

Our results, looking at magnetars, pulsars, and XRBs on the Milky Way's light, show that Galactic neutron stars are consistent with FRB locations on their hosts. This result holds across various types of comparison (distance to the star-forming region, host offset, enclosed flux, and fraction of light), although the significance varies

substantially between these. Other extragalactic transients are also consistent with the Milky Way neutron star distribution, depending on the comparison made, but FRBs are the transient most frequently in agreement. Our results cannot differentiate between most FRB progenitor models that invoke neutron stars (e.g. magnetars from core-collapse and accretion-induced collapse, ultra luminous XRBs, combing models etc; Margalit et al. 2019; Ioka & Zhang 2020; Lu, Kumar & Zhang 2020; Deng, Zhong & Dai 2021; Sridhar et al. 2021; Zhao et al. 2021). If FRBs do arise from neutron star systems, we disfavour the scenario where they originate from nascent magnetars born in LGRBs or SLSNe (see also Heintz et al. 2020; Mannings et al. 2021). A caveat is that the Milky Way would be an atypical LGRB or SLSN host galaxy, so the current Galactic magnetar population may not have arisen through this pathway. Furthermore, the stellar masses and SFRs of FRB hosts are also, on average, similar to the Milky Way (Bhandari et al. 2020; Heintz et al. 2020; Li & Zhang 2020).

It is interesting to note that the Galactic neutron star population is less consistent with CCSNe than FRBs, perhaps surprising given that CCSNe are expected to be the dominant production channel for neutron stars. This could be reflecting the offset between where supernovae occur and where neutron stars are observed. Given typical natal kick velocities (e.g. Hobbs et al. 2005; Bray & Eldridge 2016), for young magnetars (ages $\sim 10^3$–10^5 yr) this is expected to be a small distance, but it could be hundreds of parsec for XRBs. Indeed, this has been used to argue for a XRB-like origin for FRB 180916B, which lies $\sim$250 pc from a nearby star-forming region in its host (Tendulkar et al. 2021).

Alternative pathways have also been put forward, particularly for magnetar production, including merger and accretion-induced collapse of white dwarfs (Margalit et al. 2019). The recent discovery of repeating FRBs in a host galaxy dominated by a $\sim$ Gyr old stellar population (FRB 20201124A; Fong et al. 2021), and in a globular cluster (FRB 20200120E; Kirsten et al. 2021), suggests that at least some FRB progenitors/magnetars have long delay times.

Finally, we acknowledge that the FRB host sample is currently small and therefore statistical consistency with other data by means of an AD-test is more likely (or rather, it is harder to rule out). This does not diminish the results summarized in Table 6 but reflects the limitations of the current data sets. Looking solely at Table 6, neutron star systems appear to be a more plausible origin for FRBs than for other transients (if we were to ignore all other knowledge that we have about the nature of the other transients). To increase the significance of this study's results, we require better accuracy and precision in Galactic neutron star distance measurements, a deeper understanding of the biases affecting these samples, and a larger sample of FRB hosts. In future, it may be possible to use these methods to determine not only whether extragalactic FRBs arise from neutron stars but which specific systems are the progenitors. The apparent difference between single and repeating bursts (Pleunis et al. 2021) could also be investigated in this way, both in terms of their global host properties, and the environments sampled within them.

7 CONCLUSIONS

Motivated by the possibility that magnetar activity is the origin of FRBs, we have created an image of the Milky Way, simulating its face-on appearance from an extragalactic distance. We then placed magnetar, pulsar, and XRB populations on the image, according to their best distance estimates, and measured how these systems are distributed with respect to Galactic light in terms of Galactocentric offsets, host-normalized offsets, enclosed fluxes, and the fraction of light statistic. Distributions of these measurements for extragalactic transients, including FRBs, are compared to the Galactic neutron star results with AD-tests. There are $\sim$20–30 AD-tests for each transient, across the range of Galactic populations and literature measurements available for each. We find that Galactic neutron stars are distributed on the Milky Way in a similar manner to FRBs on their hosts, with 75 per cent of AD-tests returning a p-value >0.05. FRBs also stand out as being in better agreement with the Galactic neutron star population than other extragalactic transients. These results appear robust against incompleteness, uncertainties in Galaxy modelling, and distance uncertainties. We cannot distinguish whether isolated magnetars or accreting/interacting binaries containing a neutron star are the best match, but nevertheless, these results provide further support for FRB source models that invoke neutron star systems.

To make further progress with this method for understanding FRBs, an improved understanding of distance uncertainties and incompleteness in Galactic neutron star populations is required. Larger FRB host samples will also be key but this population will surely grow over the coming years.

ACKNOWLEDGEMENTS

AAC is supported by the Radboud Excellence Initiative. AJL has received funding from the European Research Council (ERC) under the European Union's Seventh Framework Programme (FP7-2007-2013) (Grant agreement No. 725246). JDL acknowledges support from a UK Research and Innovation Fellowship (MR/T020784/1). This work has made use of IPYTHON (Perez & Granger 2007), NUMPY (Harris et al. 2020), SCIPY (Virtanen et al. 2020); MATPLOTLIB (Hunter 2007), and ASTROPY,[4] a community-developed core PYTHON package for Astronomy (Astropy Collaboration 2013; Price-Whelan et al. 2018). We have also made use of Ned Wright's cosmology calculator Wright (2006). Finally, we thank the referee for their constructive feedback, which has substantially improved the clarity of this manuscript.

DATA AVAILABILITY

The input masers used in this paper were selected from the rms survey (Urquhart et al. 2014). Their distances were calculated using version 2 of the parallax-based BeSSel (Brunthaler et al. 2011) distance calculator (Reid et al. 2016, 2019), available at https://bessel.vlbi-astrometry.org/node/378. Neutron star data were obtained from the McGill catalogue (for magnetars, Olausen & Kaspi 2014), available at https://www.physics.mcgill.ca/~pulsar/magnetar/main; the ANTF data base (for pulsars; Manchester et al. 2005), available at https://www.atnf.csiro.au/research/pulsar/psrcat; Sazonov et al. (2020, for LMXBs) and Kretschmar et al. (2019, for HMXBs).

We have made interactive PYTHON scripts and notebooks available online, which generate the $F_{\rm light}$ results presented in this paper, but also allow the user to change various parameters. Along with images of the Galaxy in fits format, these can be accessed at https://github.com/achrimes2/MW-NS-Flight. Also available in this repository are the $F_{\rm light}$, offset, and enclosed flux values for the magnetar, pulsar, and XRB samples used in this paper. These data can also be found on the journal website as supplementary materials.

[4] https://www.astropy.org

REFERENCES

Abbott B. P. et al., 2017, ApJ, 848, L12
Anderson J. P., James P. A., 2009, MNRAS, 399, 559
Anderson L. D., Bania T. M., Balser D. S., Rood R. T., 2012, ApJ, 754, 62
Anderson J. P., James P. A., Habergham S. M., Galbany L., Kuncarayakti H., 2015, Publ. Astron. Soc. Aust., 32, e019
Arnason R. M., Papei H., Barmby P., Bahramian A., Gorski M. D., 2021, MNRAS, 502, 5455
Astropy Collaboration, 2013, A&A, 558, A33
Audcent-Ross F. M., Meurer G. R., Audcent J. R., Ryder S. D., Wong O. I., Phan J., Williamson A., Kim J. H., 2020, MNRAS, 492, 848
Bailes M. et al., 2021, MNRAS, 503, 5367
Baring M. G., Wadiasingh Z., Gonthier P. L., Harding A. K., Hu K., 2021, Proceedings of Science, Proc. High Energy Astrophysics in Southern Africa. p. 36
Barthelmy S. D. et al., 2005, Nature, 438, 994
Beniamini P., Hotokezaka K., van der Horst A., Kouveliotou C., 2019, MNRAS, 487, 1426
Beniamini P., Wadiasingh Z., Metzger B. D., 2020, MNRAS, 496, 3390
Bhandari S. et al., 2020, ApJ, 895, L37
Bhardwaj M. et al., 2021, ApJ, 910, L18
Binney J., Gerhard O., Spergel D., 1997, MNRAS, 288, 365
Blanchard P. K., Berger E., Fong W.-f., 2016, ApJ, 817, 144
Bland-Hawthorn J., Gerhard O., 2016, ARA&A, 54, 529
Bochenek C. D., Ravi V., Belov K. V., Hallinan G., Kocz J., Kulkarni S. R., McKenna D. L., 2020, Nature, 587, 59
Bochenek C. D., Ravi V., Dong D., 2021, ApJ, 907, L31
Bodaghee A. et al., 2007, A&A, 467, 585
Bodaghee A., Tomsick J. A., Rodriguez J., James J. B., 2012, ApJ, 744, 108
Bray J. C., Eldridge J. J., 2016, MNRAS, 461, 3747
Brunthaler A. et al., 2011, Astron. Nachr., 332, 461
Burns E. et al., 2021, ApJ, 907, L28
Castro-Ginard A. et al., 2021, A&A, 652, A162
Chatterjee S., 2020, preprint (arXiv:2012.10377)
CHIME/FRB Collaboration, 2020, Nature, 587, 54
Church R. P., Levan A. J., Davies M. B., Tanvir N., 2011, MNRAS, 413, 2004
Churchwell E. et al., 2009, PASP, 121, 213
Coleiro A., Chaty S., 2013, ApJ, 764, 185
Cordes J. M., Lazio T. J. W., 2002, preprint (astro-ph/0207156)
De K. et al., 2020a, ApJ, 901, L7
De K. et al., 2020b, ApJ, 905, 58
Deng C.-M., Zhong S.-Q., Dai Z.-G., 2021, preprint (arXiv:2102.06796)
Díaz-García S., Salo H., Knapen J. H., Herrera-Endoqui M., 2019, A&A, 631, A94
Duncan R. C., Thompson C., 1992, ApJ, 392, L9
Eftekhari T., Berger E., 2017, ApJ, 849, 162
Fahlman G. G., Gregory P. C., 1981, Nature, 293, 202
Faucher-Giguère C.-A., Kaspi V. M., 2006, ApJ, 643, 332
Flynn C., Holmberg J., Portinari L., Fuchs B., Jahreiß H., 2006, MNRAS, 372, 1149
Fong W., Berger E., Fox D. B., 2010, ApJ, 708, 9
Fong W. et al., 2013, ApJ, 769, 56
Fong W.-f. et al., 2021, preprint (arXiv:2106.11993)
Fruchter A. S. et al., 2006, Nature, 441, 463
Gaia Collaboration, 2016, A&A, 595, A1
Gardenier D. W., van Leeuwen J., 2021, A&A, 651, A63
Grady J., Belokurov V., Evans N. W., 2020, MNRAS, 492, 3128
Gravity Collaboration, 2019, A&A, 625, L10
Green J. A. et al., 2017, MNRAS, 469, 1383
Grossan B., 2021, PASP, 133, 074202
Gullón M., Pons J. A., Miralles J. A., Viganò D., Rea N., Perna R., 2015, MNRAS, 454, 615
Harris C. R. et al., 2020, Nature, 585, 357
Heintz K. E. et al., 2020, ApJ, 903, 152
Hilmarsson G. H. et al., 2020, MNRAS, 493, 5170
Hobbs G., Lorimer D. R., Lyne A. G., Kramer M., 2005, MNRAS, 360, 974
Hou L. G., Han J. L., 2014, A&A, 569, A125
Hunter J. D., 2007, Comput. Sci. Eng., 9, 90
Hurley K. et al., 2005, Nature, 434, 1098
Ioka K., Zhang B., 2020, ApJ, 893, L26
James P. A., Anderson J. P., 2006, A&A, 453, 57
James C. W., Prochaska J. X., Macquart J. P., North-Hickey F., Bannister K. W., Dunning A., 2021, preprint (arXiv:2101.08005)
Jonker P. G., Nelemans G., 2004, MNRAS, 354, 355
Kasen D., Bildsten L., 2010, ApJ, 717, 245
Katz J. I., 2016, ApJ, 826, 226
Keane E. F., 2018, Nat. Astron., 2, 865
Kelly P. L., Kirshner R. P., 2012, ApJ, 759, 107
Kirsten F. et al., 2021, preprint (arXiv:2105.11445)
Kouveliotou C. et al., 1998, Nature, 393, 235
Kretschmar P. et al., 2019, New Astron. Rev., 86, 101546
Krivonos R. A., Tsygankov S. S., Mereminskiy I. A., Lutovinov A. A., Sazonov S. Y., Sunyaev R. A., 2017, MNRAS, 470, 512
Levan A. J., Wynn G. A., Chapman R., Davies M. B., King A. R., Priddey R. S., Tanvir N. R., 2006, MNRAS, 368, L1
Li D., Zanazzi J. J., 2021, ApJ, 909, L25
Li Y., Zhang B., 2020, ApJ, 899, L6
Li C. K. et al., 2021, Nat. Astron., 5, 378
Licquia T. C., Newman J. A., Brinchmann J., 2015, ApJ, 809, 96
Lin L. et al., 2020, Nature, 587, 63
Lu W., Kumar P., Zhang B., 2020, MNRAS, 498, 1397
Lumsden S. L., Hoare M. G., Urquhart J. S., Oudmaijer R. D., Davies B., Mottram J. C., Cooper H. D. B., Moore T. J. T., 2013, ApJS, 208, 11
Lunnan R. et al., 2015, ApJ, 804, 90
Lunnan R. et al., 2017, ApJ, 836, 60
Luo R., Men Y., Lee K., Wang W., Lorimer D. R., Zhang B., 2020, MNRAS, 494, 665
Lyman J. D. et al., 2017, MNRAS, 467, 1795
Manchester R. N., Hobbs G. B., Teoh A., Hobbs M., 2005, AJ, 129, 1993
Manchester R. N., Hobbs G. B., Teoh A., Hobbs M., 2016, VizieR Online Data Catalog, B/psr
Mannings A. G. et al., 2021, ApJ, 917, 75
Margalit B., Berger E., Metzger B. D., 2019, ApJ, 886, 110
Margalit B., Beniamini P., Sridhar N., Metzger B. D., 2020, ApJ, 899, L27
Mazets E. P., Golenetskij S. V., Guryan Y. A., 1979a, Sov. Astron. Lett., 5, 343
Mazets E. P., Golentskii S. V., Ilinskii V. N., Aptekar R. L., Guryan I. A., 1979b, Nature, 282, 587
Metzger B. D., Quataert E., Thompson T. A., 2008, MNRAS, 385, 1455
Metzger B. D., Giannios D., Thompson T. A., Bucciantini N., Quataert E., 2011, MNRAS, 413, 2031
Metzger B. D., Berger E., Margalit B., 2017, ApJ, 841, 14
Mondal S., Bera A., Chandra P., Das B., 2020, MNRAS, 498, 3863
Nuñez C. et al., 2021, A&A, 653, A119
Ofek E. O. et al., 2006, ApJ, 652, 507
Ofek E. O. et al., 2008, ApJ, 681, 1464
Olausen S. A., Kaspi V. M., 2014, ApJS, 212, 6
Palliyaguru N. T., Agarwal D., Golpayegani G., Lynch R., Lorimer D. R., Nguyen B., Corsi A., Burke-Spolaor S., 2021, MNRAS, 501, 541
Pastor-Marazuela I. et al., 2020, preprint (arXiv:2012.08348)
Perets H. B., Beniamini P., 2021, MNRAS, 503, 5997
Perez F., Granger B. E., 2007, Comput. Sci. Eng., 9, 21
Pestalozzi M. R., Minier V., Booth R. S., 2005, A&A, 432, 737
Platts E., Weltman A., Walters A., Tendulkar S. P., Gordin J. E. B., Kandhai S., 2019, Phys. Rep., 821, 1
Pleunis Z. et al., 2021, preprint (arXiv:2106.04356)
Price-Whelan A. M. et al., 2018, AJ, 156, 123
Rajwade K. M., Lorimer D. R., Anderson L. D., 2017, MNRAS, 471, 730
Reid M. J. et al., 2014, ApJ, 783, 130
Reid M. J., Dame T. M., Menten K. M., Brunthaler A., 2016, ApJ, 823, 77
Reid M. J. et al., 2019, ApJ, 885, 131
Repetto S., Igoshev A. P., Nelemans G., 2017, MNRAS, 467, 298
Ridnaia A. et al., 2021, Nat. Astron., 5, 372
Russeil D., 2003, A&A, 397, 133

Safarzadeh M., Prochaska J. X., Heintz K. E., Fong W.-f., 2020, ApJ, 905, L30
Sartore N., Ripamonti E., Treves A., Turolla R., 2010, A&A, 510, A23
Sazonov S. et al., 2020, New Astron. Rev., 88, 101536
Schulze S. et al., 2021, ApJS, 255, 29
Seigar M. S., James P. A., 1998, MNRAS, 299, 685
Sharma S., Bland-Hawthorn J., Johnston K. V., Binney J., 2011, ApJ, 730, 3
Sridhar N., Metzger B. D., Beniamini P., Margalit B., Renzo M., Sironi L., Kovlakas K., 2021, ApJ, 917, 13
Svensson K. M., Levan A. J., Tanvir N. R., Fruchter A. S., Strolger L.-G., 2010, MNRAS, 405, 57
Svinkin D. et al., 2021, Nature, 589, 211
Tavani M. et al., 2021, Nat. Astron., 5, 401
Tendulkar S. P. et al., 2021, ApJ, 908, L12
The CHIME/FRB Collaboration, 2021, preprint (arXiv:2106.04352)
Thompson C., Duncan R. C., 1996, ApJ, 473, 322
Tunnicliffe R. L. et al., 2014, MNRAS, 437, 1495
Uddin S. A. et al., 2020, ApJ, 901, 143
Urquhart J. S., Figura C. C., Moore T. J. T., Hoare M. G., Lumsden S. L., Mottram J. C., Thompson M. A., Oudmaijer R. D., 2014, MNRAS, 437, 1791
Usov V. V., 1992, Nature, 357, 472
Valdettaro R. et al., 2001, A&A, 368, 845
Vallée J. P., 2002, ApJ, 566, 261
Vallée J. P., 2008, AJ, 135, 1301
Vallée J. P., 2014, AJ, 148, 5
van Paradijs J., White N., 1995, ApJ, 447, L33
Verberne S., Vink J., 2021, MNRAS, 504, 1536
Verrecchia F. et al., 2021, ApJ, 915, 102
Virtanen P. et al., 2020, Nat. Meth., 17, 261
Wang X., Wang L., Filippenko A. V., Zhang T., Zhao X., 2013, Science, 340, 170
White N. E., van Paradijs J., 1996, ApJ, 473, L25
Widrow L. M., Pym B., Dubinski J., 2008, ApJ, 679, 1239
Winkler C. et al., 2003, A&A, 411, L1
Wisnioski E., Glazebrook K., Blake C., Poole G. B., Green A. W., Wyder T., Martin C., 2012, MNRAS, 422, 3339
Woosley S. E., 2010, ApJ, 719, L204
Wright E. L., 2006, PASP, 118, 1711
Xiao D., Wang F., Dai Z., 2021, Sci. China Phys. Mech. Astron., 64, 249501
Yao J. M., Manchester R. N., Wang N., 2017, ApJ, 835, 29
Younes G. et al., 2021, Nat. Astron., 5, 408
Yu S.-Y., Ho L. C., 2020, ApJ, 900, 150
Yu S.-Y., Ho L. C., Barth A. J., Li Z.-Y., 2018, ApJ, 862, 13
Yusifov I., Küçük I., 2004, A&A, 422, 545
Zari E., Rix H.-W., Frankel N., Xiang M., Poggio E., Drimmel R., Tkachenko A., 2021, A&A, 650, A112
Zhang B., 2020, Nature, 587, 45
Zhao Z. Y., Zhang G. Q., Wang Y. Y., Tu Z.-L., Wang F. Y., 2021, ApJ, 907, 111

SUPPORTING INFORMATION

Supplementary data are available at *MNRAS* online.

Table A2. An extract of a table containing offset, enclosed flux, and $F_{\rm light}$ results for the pulsar sample.

Please note: Oxford University Press is not responsible for the content or functionality of any supporting materials supplied by the authors. Any queries (other than missing material) should be directed to the corresponding author for the article.

APPENDIX A: MILKY WAY MAGNETAR MEASUREMENTS

In Table A1 of this appendix, we provide a table of measurements for the 20 Milky Way magnetars that lie this side of GC ($y < 8.3$ kpc on our map). The measurements are typical of those used in extragalactic transient studies, including host offset, host-normalized offset, $F_{\rm light}$, and the enclosed flux fraction at their radius. The heliocentric distances, their uncertainties, and the type of measurement are also provided (partially reproduced from the McGill magnetar catalogue; Olausen & Kaspi 2014).

Table A2 contains the same offset, enclosed flux, and fraction of light data for the pulsar and XRB samples. Only a subset of pulsar data is shown here, the full results for all samples are available at https://github.com/achrimes2/MW-NS-Flight or as supplementary materials on the journal website. These results can be used in future comparative studies.

Table A1. The 20 magnetars that satisfy the criteria of having (i) a distance estimate and (ii) lying at $y < 8.3$ kpc. Magnetar distance information is from the McGill catalogue (Olausen & Kaspi 2014, and reference therein). The $F_{\rm light}$ values are calculated using a 12 kpc pixel selection radius and pixels from the whole Galaxy.

Magnetar	Dist./Assoc.	$d_\odot$ (kpc)	δr (kpc)	$\delta r/r_{\rm e}$ (B)	$\delta r/r_e$ (I)	$F_{\rm light}$ (B)	$F_{\rm light}$ (I)	$F_{\rm enc}$ (B)	$F_{\rm enc}$ (I)
4U0142+61	RC	$3.6^{+0.4}_{+0.4}$	10.85	4.57	4.88	0.02	0.01	0.98	0.98
SGR0418+5729	PA	∼2	9.95	4.20	4.47	0.07	0.05	0.95	0.96
SGR0501+4516	PA/SNR	∼2	10.12	4.27	4.55	0.03	0.03	0.96	0.96
1E1048.1−5937	RC	$9^{+1.7}_{-1.7}$	10.10	4.26	4.54	0.03	0.03	0.96	0.96
1E1547.0−5408	SNR	$4.5^{+0.5}_{-0.5}$	5.04	2.13	2.27	0.35	0.31	0.57	0.64
PSRJ1622−4950	DM/SNR	$9^{+1.4}_{-1.4}$	3.97	1.68	1.78	0.44	0.39	0.44	0.53
CXOUJ164710.2−455216	CA	$3.9^{+0.7}_{-0.7}$	4.75	2.00	2.14	0.37	0.32	0.54	0.61
1RXSJ170849.0−400910	RC	$3.8^{+0.5}_{-0.5}$	4.59	1.94	2.06	0.42	0.36	0.52	0.59
SGRJ1745−2900	HI	$8.3^{+0.3}_{-0.3}$	0.10	0.04	0.04	0.99	0.99	0.00	0.00
XTEJ1810−197	HI	$3.5^{+0.5}_{-0.4}$	4.81	2.03	2.16	0.34	0.31	0.54	0.61
SwiftJ1818.0−1607	DM	$4.8^{+1.65}_{-1.65}$	3.77	1.59	1.69	0.49	0.47	0.42	0.50
SwiftJ1822.3−1606	HI/HII	$1.6^{+0.3}_{-0.3}$	6.67	2.81	3.00	0.39	0.32	0.74	0.78

Table A1 – *continued*

Magnetar	Dist./Assoc.	$d_\odot$ (kpc)	δr (kpc)	$\delta r/r_e$ (B)	$\delta r/r_e$ (I)	$F_{\rm light}$ (B)	$F_{\rm light}$ (I)	$F_{\rm enc}$ (B)	$F_{\rm enc}$ (I)
SwiftJ1834.9−0846	SNR	$4.2^{+0.3}_{-0.3}$	4.65	1.96	2.09	0.38	0.34	0.52	0.59
1E1841−045	SNR	$8.5^{+1.3}_{-1}$	3.96	1.67	1.78	0.60	0.49	0.42	0.50
3XMMJ185246.6+003317	HI/SNR	∼7.1	4.54	1.92	2.04	0.41	0.36	0.49	0.57
SGR1935+2154	F/SNR	$6.5^{+3.0}_{-5.3}$	7.20	3.04	3.24	0.13	0.13	0.77	0.81
1E2259+586	SNR/PA	$3.2^{+0.2}_{-0.2}$	9.73	4.11	4.37	0.17	0.13	0.94	0.95
AXJ1845.0−0258	HI/SNR	∼8.5	4.27	1.80	1.92	0.59	0.48	0.45	0.54
SGR2013+34	HII	∼8.8	10.04	4.24	4.51	0.03	0.03	0.95	0.96
PSRJ1846−0258	SNR	$6^{+1.5}_{-0.9}$	4.22	1.78	1.90	0.46	0.42	0.46	0.54

Note. RC – distance from red clump stars, PA – Perseus arm association, SNR – supernova remnant association, DM – dispersion measure distance, CA – cluster association, H I – distance from H I column density, H II – H II region association, F – distance estimate from burst flux

Table A2. An extract of a table containing offset, enclosed flux, and $F_{\rm light}$ results for the pulsar sample. The full data for the pulsars, XRBs, and magnetars are available as .txt files on the journal website, and at https://github.com/achrimes2/MW-NS-Flight, with the same columns and in the same format as below. The $F_{\rm light}$ values quoted are for half-Galaxy measurements.

δr (kpc)	$\delta r/r_e$ (B)	$\delta r/r_e$ (I)	$F_{\rm light}$ (B)	$F_{\rm light}$ (I)	$F_{\rm enc}$ (B)	$F_{\rm enc}$ (I)
9.64	4.06	4.33	0.04	0.04	0.94	0.95
15.65	6.59	7.03	0.00	0.00	1.00	1.00
8.76	3.69	3.94	0.06	0.06	0.88	0.90
9.26	3.90	4.16	0.04	0.04	0.91	0.93
10.99	4.63	4.94	0.02	0.02	0.98	0.99

APPENDIX B: FRACTION OF LIGHT DISTRIBUTIONS FOR PULSARS AND XRBS

The fraction of light method described for the magnetars in Section 5 is repeated here for the ATNF luminous pulsars and the INTEGRAL XRBs. Their positions on the half-map, the local subregion, and the resultant $F_{\rm light}$ distributions are shown in Figs B1–B3.

In Fig. B1, the result of varying the pulsar luminosity cut shown in Fig. 1 is also demonstrated. Moving the cut within the region denoted by the dashed lines in Fig. 1, the maximum and minimum distributions that occur in this range are shaded between, demonstrating that the precise choice of cut has a minimal impact.

As for the magnetars, restricting the analysis to the local 4 kpc pushes the pulsar and HMXB distributions closer towards the 1:1 line, with the effect greater in the *I* band than the *B* band. Again, this is because these samples avoid the Galactic bulge (with an additional effect due to survey/detection biases in the pulsar case). The effect occurs to a much lesser extent for LMXBs, which being an older population, already favour the Galactic bulge.

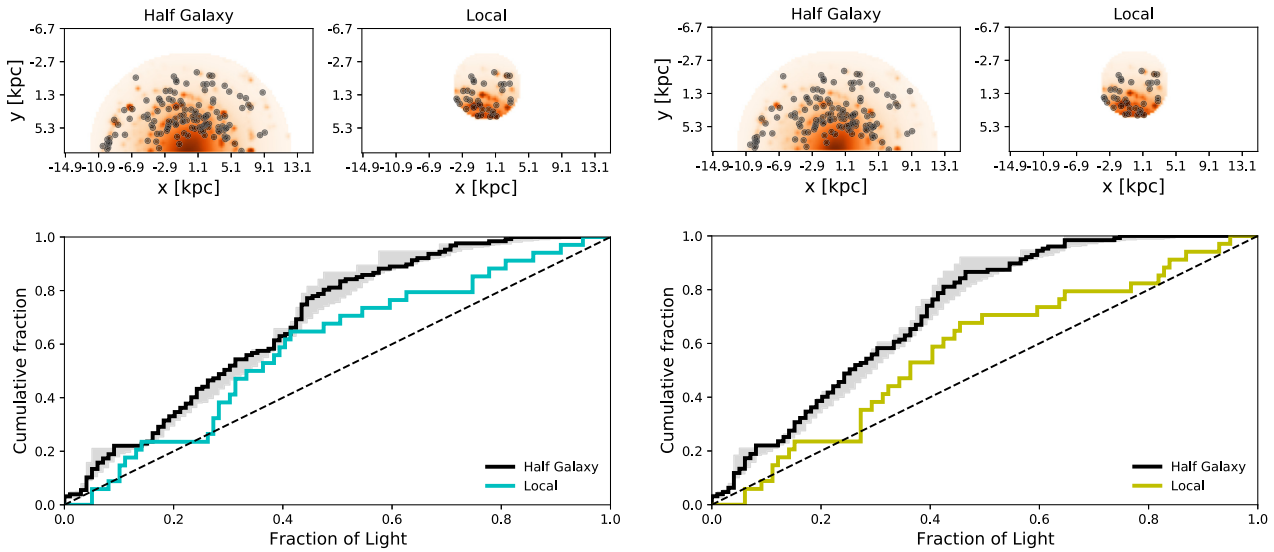

Figure B1. The same information as in Figs 8 and 9, but for the bright ANTF pulsars. Top: $F_{\rm light}$ *B*-band and *I*-band colour maps with the half-Galaxy and 4 kpc heliocentric distance restriction. The pulsar locations are indicated. Bottom: The corresponding $F_{\rm light}$ distributions. The grey shading bounds the minimum and maximum distributions that arise from varying the luminosity cut by ±0.5 dex (see Fig. 1).

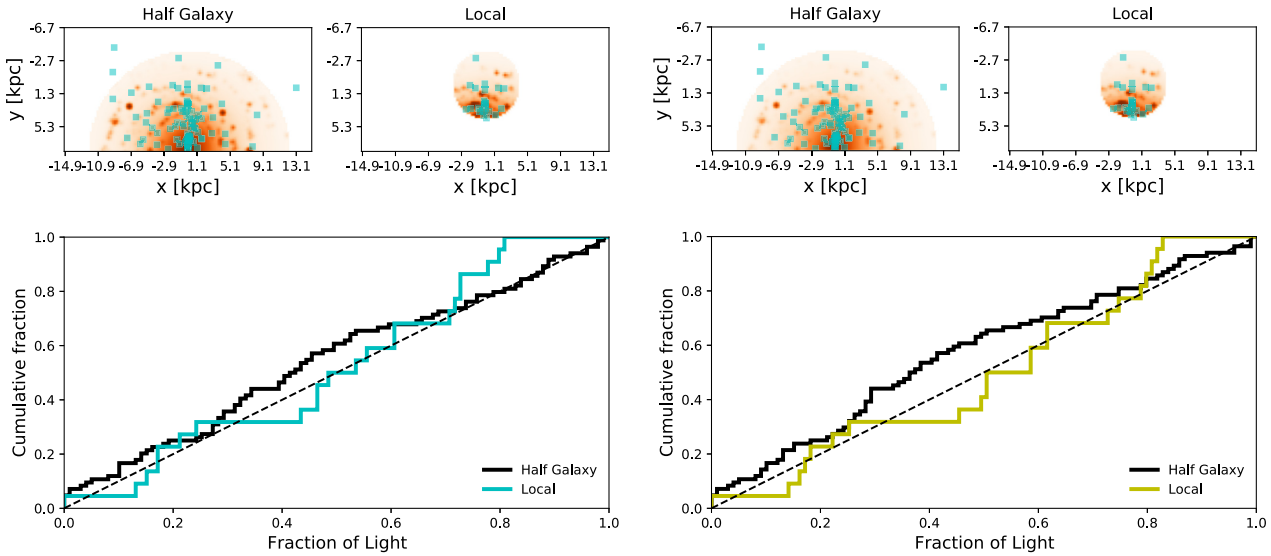

Figure B2. As in Fig. B1, but for the LMXBs. Only in the half-Galaxy case do we consider objects outside the selected pixels, assigning them $F_{\rm light} = 0$.

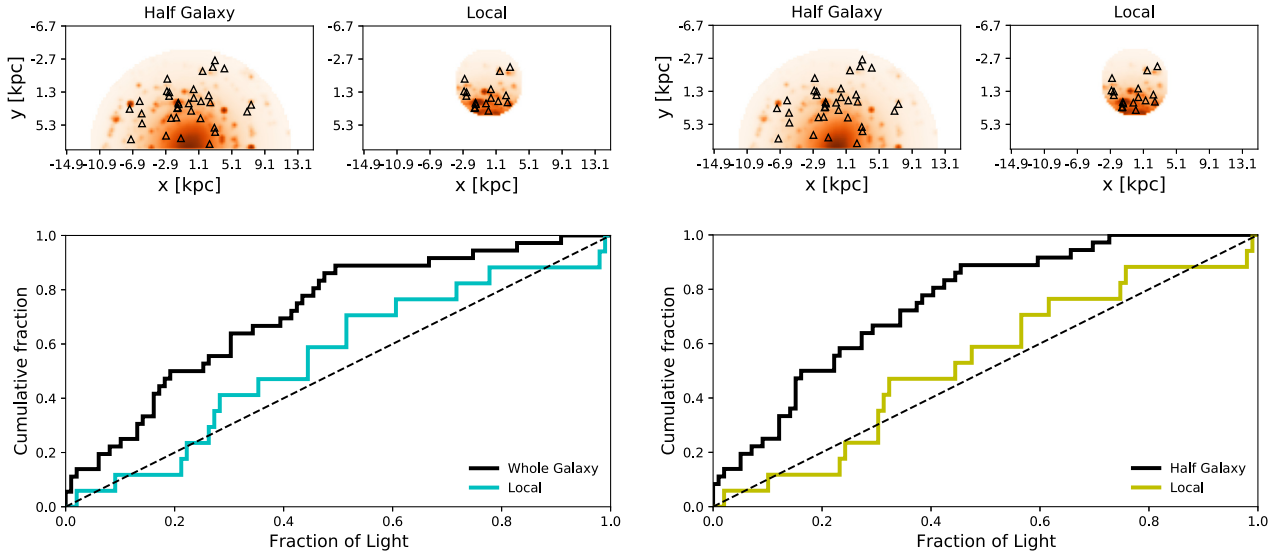

Figure B3. As in Figs B1 and B2, but for HMXBs.

This paper has been typeset from a TEX/LATEX file prepared by the author.